2012

Shear Horizontal Component Of Crack Growth Related Acoustic Emission Signals

Craig Russel Supria
North Carolina Agricultural and Technical State University

SHEAR HORIZONTAL COMPONENT OF CRACK GROWTH RELATED ACOUSTIC EMISSION SIGNALS

by

Craig Russel Supria

A thesis submitted to the graduate faculty
in partial fulfillment of the requirements for the degree of
MASTER OF SCIENCE

Department: Mechanical Engineering
Major: Mechanical Engineering
Major Professor: Dr. Mannur J. Sundaresan

North Carolina A&T State University
Greensboro, North Carolina
2012

School of Graduate Studies
North Carolina Agricultural and Technical State University

This is to certify that the Master's Thesis of

Craig Russel Supria

has met the thesis requirements of
North Carolina Agricultural and Technical State University

Greensboro, North Carolina
2012

Approved by:

Dr. Mannur J. Sundaresan Major Professor	Dr. Dhananjay Kumar Committee Member
Dr. Albert Esterline Committee Member	Dr. Samuel Owusu-Ofori Department Chairperson

Dr. Sanjiv Sarin
Associate Vice Chancellor for Research
and Dean of Graduate Studies

BIOGRAPHICAL SKETCH

Craig Russel Supria was born on August 3, 1988, in Kingston, Jamaica. He received the Bachelor of Science degree in Mechanical Engineering from North Carolina Agricultural and Technical State University in 2010. He is currently a candidate for the Master of Science degree in Mechanical Engineering.

ACKNOWLEDGMENT

I would like to thank my advisor, Dr. Mannur J. Sundaresan for his guidance and support through educational and personally challenging times during my studies at North Carolina Agricultural and Technical State University. I wish to express my appreciation to my thesis committee members, Dr. Samuel Owusu-Ofori, Dr. Dhananjay Kumar and Dr. Albert Esterline, for their time and critical review of my thesis. I also would like to acknowledge my fellow graduate students at the Intelligent Structures and Mechanisms laboratory for sharing their knowledge and providing support, but most of all their friendship. Lastly, I wish to thank my parents and brother for their constant support, encouragement and love.

TABLE OF CONTENTS

LIST OF FIGURES

FIGURE **PAGE**

LIST OF TABLES

TABLE **PAGE**

LIST OF SYMBOLS

SHM	Structural Health Monitoring
AE	Acoustic Emission
FE	Finite Element
NDE	Non Destructive Evaluation
S_0	Symmetric Mode
A_0	Antisymmetric Mode
SH	Shear Horizontal Mode
SV	Shear Vertical Mode
C_g	Group Velocity
f	Frequency
E	Modulus of Elasticity
ρ	Density of a material
ν	Poisson's Ratio
VPG	Virtual Proving Ground
MTS	Material Test System
PXE	Piezoxide

ABSTRACT

Supria, Craig Russel. SHEAR HORIZONTAL COMPONENT OF CRACK GROWTH RELATED ACOUSTIC EMISSION SIGNALS. **(Major Professor: Dr. Mannur J. Sundaresan)**, North Carolina Agricultural and Technical State University.

In this research, the acoustic emissions from simulated crack growth and incremental crack growth in a cyclically loaded aluminum panel were detected by acoustic emission sensors. One of these sensors comprised of an array of thin strips of piezoelectric material bonded to the specimen and electrically connected. The geometry of these sensor strip arrays and their orientation to the fracture site enabled the sensors to capture the shear horizontal component of the acoustic emission waveform. Cyclical loading was used to grow the crack, allowing sensor performance to be assessed and compared to bonded piezoelectric sensors and resonant frequency acoustic emission sensors.

The detection of the shear waves is of particular interest as significant amplitudes of shear horizontal component is expected only from crack growth events. Other mechanically generated stress wave signals are not expected to have recognizable shear horizontal components. Hence the new sensor can provide a means of discriminating between critical events (crack propagation) and sources of minimal concern (fretting). Shear modes were detected in the acoustic emissions from both the simulated crack growth and the crack growth due to cyclical loading.

CHAPTER 1

INTRODUCTION

1.1 Structural Health Monitoring

Structural health monitoring (SHM) are useful in monitoring the initiation and growth of damage in critical locations of structural members. Damages such as fatigue cracks in metals and delaminations in composite structures adversely affect the structural integrity. Aerospace structures continuously undergo fatigue damage during service which eventually leads to catastrophic failure if not detected and repaired. There are various techniques that can detect threats in a structure (Chang, United States. Air Force. Office of Scientific Research., United States. Army Research Office, & National Science Foundation (U.S.), 1997). Some of these SHM techniques are fiber optics, acoustic emission technique and stress wave propagation. Usually sensor arrays are used to monitor and measure the health of a structure or the response of test articles to simulated loading conditions in the laboratory. The signals from the sensors analyzed to determine the extent of damage and estimate the reliability of the structure.

Early detection of damage can improve the save lives and reduce operational cost. Damage detection traditionally involves performing periodic maintenance and inspections after adverse events. These inspections are typically very costly and time consuming which is an inconvenience to owners and users alike. Detailed inspections of aircrafts for example may involve the disassembly of the wing, tail and fuselage in order to gain access to the inner sections where critical damage may potentially occur.

Structural health monitoring however uses noninvasive methods that can continually monitor critical regions of the structure during service.

Structural health monitoring offers the following advantages to any given structure:

i. Implements state of the art approaches for damage detection, location and assessment
ii. Reduces downtime by targeting inspections to suspect regions instead of the entire structure
iii. Offers real time SHM for critical infrastructure

A classification of the functional categories of SHM applications are:

i. Transportation: airports, bridges and rail and transit
ii. Lifeline systems: power plants, water plants and communication towers
iii. Buildings: stadiums, high-rises, towers
iv. Other structures: off shore platforms, wind turbines, tunnels

1.2 Acoustic Emission

Acoustic emission (AE) is the rapid release of energy from localized sources such as deformation, crack propagation and dislocation that generates elastic waves which propagates throughout the material (Graff, 1991). These elastic waves or acoustic energy are detected on the surface of the structure using various sensing elements such as piezoelectric transducers and converted into acoustic emission signals. These acoustic signals may appear as discrete pulses or as a continuous signal. AE differs from most

non-destructive evaluation techniques as the acoustic energy detected is generated from the incremental damage itself instead of being provided by an external source such as in the case of ultrasonic technique. Further, acoustic emission technique is able to detect the rate of damage growth.

Acoustic emission signals are generated from various deformation mechanisms and fracture. In metals for example, sources may include the sliding of the grain boundary, crack growth and plastic deformation. On the other hand in composite materials, sources include delamination, matrix cracking and fiber fractures.

There are several distinct advantages offered by AE technique such as the its ability to quickly locate and rate damage growth in a complex part while the part is in service. The acoustic emission technique however has been hampered by the presence of spurious signals from sources such as micron scale movement of surfaces fastened together with bolts or rivets. These acoustic emissions from these fretting sources have historically led to false positives that diminish the confidence in the acoustic emission technique.

Numerical simulations and experiments performed in our research group have shown the presence of the shear mode in acoustic emissions generated by incremental crack growth. In the simulations, the shear horizontal component of guided wave was found to be a dominant component in the waveform sensed at most angles of incidence between the emission source and the sensor. Further, other mechanical sources of acoustic emission such as frictional sliding are not expected to result in such shear horizontal component in the waveform.

These two findings in combination have prompted suggest the need for the development of sensors that are capable of isolating shear horizontal component of the AE signals while being insensitive to the symmetric and antisymmetric modes of the waveform. Such a sensor is expected to be valuable for minimizing the false positives in acoustic emission data. The approach taken in designing these sensors was to (a) bond piezoelectric strips to the specimen surface to enable detection of the shear wave, (b) use a high aspect ratio strips targeted to acquiring the shear component, and (c) connect an array of the strips together to generate a reliable voltage output.

1.3 Objectives

The objectives of this thesis are:

a) To understand wave propagations and the different guided wave modes caused by incremental crack growth in thin aluminum plates

b) To understand and evaluate the shear horizontal component of crack growth that is related to incremental fatigue crack growth

c) To develop and evaluate the performance of a sensor capable of isolating shear horizontal component in the AE signals

CHAPTER 2

LITERATURE REVIEW

2.1 Introduction

Acoustic emission, which is the rapid release of energy from localized sources, generates elastic waves that propagate throughout a structure or a material (Mickens et al., 2003). Therefore, it is important to understand the theory of wave propagation and the many different patterns involved with these waveforms that are related to acoustics and ultrasonic testing. Giurgiutiu et al (2003). studied the different types of wave propagation through beam and plate structures using active sensors. Wave propagates in four principle modes in solids which are based on the way the particles vibrate. The wave can propagate as longitudinal wave, shear wave, surface wave, and in thin materials as plate waves (Giurgiutiu, Bao, & Zhao, 2003). Table 2.1, which is shown below, summarizes the wave modes that are possible in solid materials.

Table 2.1. Wave modes in solids summarization

Wave Types in Solids	Particle Vibrations
Longitudinal/Compressional wave	Parallel to the direction of wave propagation
Transverse/Shear/Distortional wave	Perpendicular to the direction of wave propagation
Surface/Rayleigh wave	Elliptical orbit - symmetrical mode
Plate/Lamb wave	Complex pattern of longitudinal and transverse movement

2.2 Acoustic Emission Waveform Signals

The dominant wave that propagates throughout thin plates, are Lamb waves which are sometimes referred to as plate waves. The theory of Lamb waves was originally developed by Horace Lamb in 1916 to describe the characteristics of waves propagating in plates (Lamb, 1904). Lamb waves can be divided into three types, each of which has an infinite number of modes. The first type is the symmetric (or extensional) waves referred to as S_n, where n refers to the order of the mode, that causes average displacement of particles over the thickness of the plate predominantly in the longitudinal direction (the direction of the wave propagation). The second type is the antisymmetric (or flexural) mode referred to as A_n, that causes average displacement of particles in the transverse direction of the wave propagation. The third type is the shear horizontal or SH mode, which causes particle oscillations that are horizontal to the plane or plate. The SH mode can either be symmetric or antisymmetric with respect to the mid-plane. All three types of waves have an infinite number of modes which are dispersive. This means that the velocity of the mode is dependent on the frequency of the wave. Symmetric modes travel at a faster speed than the antisymmetric mode which spreads through a plate. with a short impulse that is usually of duration less than 1 microsecond from the source.

Acoustic emission waveforms have specific features and using these features inferences can be made about the sources of the emissions and the source strength. While monitoring structures acoustic emission features can indicate the type of damage and the extent of damage. A typical AE waveform along with a description of some of these parameters is shown in Figure 2.1.

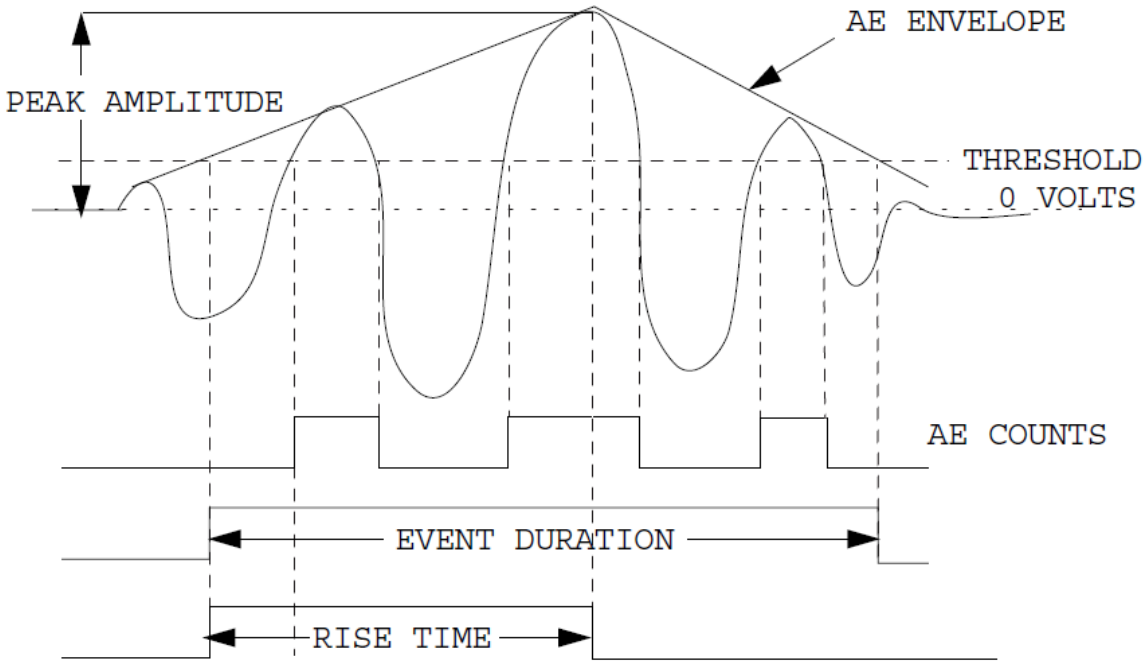

Figure 2.1. Typical Acoustic Emission waveform, (Graff, 1991)

Peak Amplitude - Maximum voltage level of the AE event.

Duration - The length of time that the event remains above the threshold once detected.

Counts - The number of times that the event crosses the threshold of the system.

Energy - The area under the AE envelope.

Rise Time - The time it takes an AE event to reach its peak amplitude, once detected.

Gorman et al (1991). delineated how the symmetric and antisymmetric mode from acoustic emission signals can be generated using pencil lead breaks on aluminum and composite structures (Gorman, 1991) . Dunegan (1981) reported that pencil lead break on the surface of a plate duplicates noise sources such as impact and friction while the pencil lead break on the edge of the plate duplicates crack growth related sources (Dunegan,

Hartman, & American Society for Nondestructive Testing., 1981). Gorman also applied Lamb wave equations for interpreting acoustic emission signals (Gorman, 1991), based on the theory developed by Worlton (Worlton, 1961).

Grondel et al (2002). developed damage detection integrated systems to monitor fatigue crack of riveted aluminum strap joints by means of Lamb wave analysis and AE measurement techniques during cyclical loading (Grondel, Delebarre, Assaad, Dupuis, & Reithler, 2002). Lamb waves are generated on one side of the riveted joint and received on the opposite side, and Hilbert transform and time-frequency analysis of the received signal was performed. Results showed that the combination of Lamb wave and AE analyses, the damage development in the riveted joint could be quantified. Viktorov's analytical model describes dispersion curves that illustrate plate mode phase velocities and group velocities as a function of frequency thickness (Viktorov, 1967). Viktorov's analysis indicates that S_0 and A_0 modes are less dispersive below in the regime in which the frequency x thickness product is below 800 kHz mm.

The time frequency analysis is based on the use of Fourier transform and has been applied on the received signal *x(t)* as shown in equation 2.1,

$$S(t,f) = \int_{-\infty}^{+\infty} x(u)h(u-f)e^{-i2\pi fu}du \tag{2.1}$$

where *h(t)* signifies the sliding window and *f* is the frequency. The Hilbert transform *x(t)* of a function *x(t)* is defined for all *t* in equation 2.2

$$\hat{x}(t) = \frac{1}{\pi}\int_{-\infty}^{+\infty} x(u)\frac{1}{t-u}du \tag{2.2}$$

2.3 Group Velocity Concept

Group velocity is associated with the propagation velocity of a group of waves of similar frequency. According to Lord Rayleigh (Rose, 1999), "It has often been remarked that when a group of waves advances into still water, the velocity of the group is less than that of the individual waves of which it is composed; the waves appear to advance through the group, dying away as they approach its interior limit".

Wang and Yuan, examined the group velocity and characteristic wave curves of Lamb waves in composites by through analytical models and experiments (Wang & Yuan, 2007).

2.4 Horizontal Shear Component

Shear wave propagation are quite intriguing and very valuable for applications involving wave propagation which includes ultrasonic non-destructive evaluation. There are two forms of shear waves which are shear vertical (SV) and shear horizontal (SH) waves. Traditionally, the longitudinal and vertical shear modes of wave propagation have been the most commonly used because they are simple to understand and to generate. Yet horizontal shear waves can also be generated quite easily through a variety of different transducers. The term "horizontal shear" means that the particle vibrations (displacements and velocities) caused by any of the SH modes are in a plane that is parallel to the surface of the plate. Figure 2.2 shows the wave propagating in the x_1 direction and the particle displacements are in the x_3 direction.

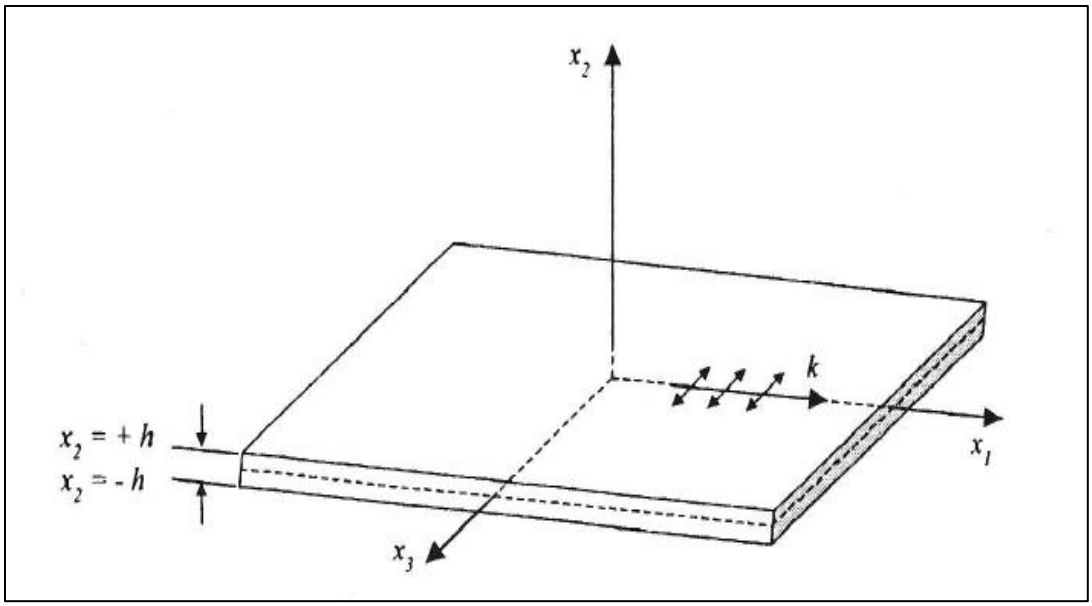

Figure 2.2. SH wave mode propagation, where the propagation is along x_1 and particle displacements are along x_3 (Rose, 1999)

Miller and Wood provided a detailed analysis of the different stress wave components generated by an impulse at the surface of a semi-infinite space and determined the percentage of energy partitioned between the longitudinal, shear, and surface wave components as 7%, 26%, and 67%, respectively (Miller & Pursey, 1955).

Detailed analysis of stress waves generated by transient events similar to crack growth in semi-infinite media as well as in plane strain conditions has been available for some time (N. E. Dowling, 2009). The stress waves generated by these sources include longitudinal and shear wave components. Further, the stress wave energy carried by the shear component appears to be significantly larger than the longitudinal component in a semi-infinite medium.

2.4.1 Phase Velocities and Cutoff Frequencies

The explicit solutions of the dispersion equation of any mode specified by the integer *n* can be determined and from this equation, the phase velocity (C_p) can be solved (Thyagarajan, Schulz, Pai, & Chung, 1998). The dispersion equation 2.3 is written as

$$\frac{\omega^2}{{c_T}^2} - k^2 = \left(\frac{n\pi}{2h}\right)^2 \tag{2.3}$$

where C_T is the shear velocity, ω is the circular frequency, *k* is the wave number of the mode ($k = \omega/c_p = 2\pi/\lambda$) and *2h* is the thickness of the material. Substituting and rearranging equation 2.3, phase velocity C_p is solved in terms of the frequency thickness product *fd*, where $d = 2h$ and $\omega = 2\pi f$. The result is shown in equation 2.4 below.

$$c_p(fd) = \pm 2c_T \left\{\frac{fd}{\sqrt{4(fd)^2 - n^2{c_T}^2}}\right\} \tag{2.4}$$

It is to be noted that for the zeroth order symmetric SH mode (when $n = 0$) the phase velocity is equal to the shear velocity, a dispersionless wave propagating at the shear wave speed C_T. All other shear horizontal modes are dispersive (i.e., for all $n \neq 0$).

The cutoff frequencies of the SH modes can be found by setting the denominator in equation 2.4 to zero. This equates to infinite phase and zero group velocities. The *n*th cutoff frequency is given in equation 2.5.

$$(fd)_n = \frac{nc_T}{2} \tag{2.5}$$

Figure 2.3 shows the phase velocity dispersion curves for the first eight SH modes over a frequency thickness range of 0-15 MHz-mm. The solid curves denote symmetric modes while the dashed curves represent antisymmetric modes.

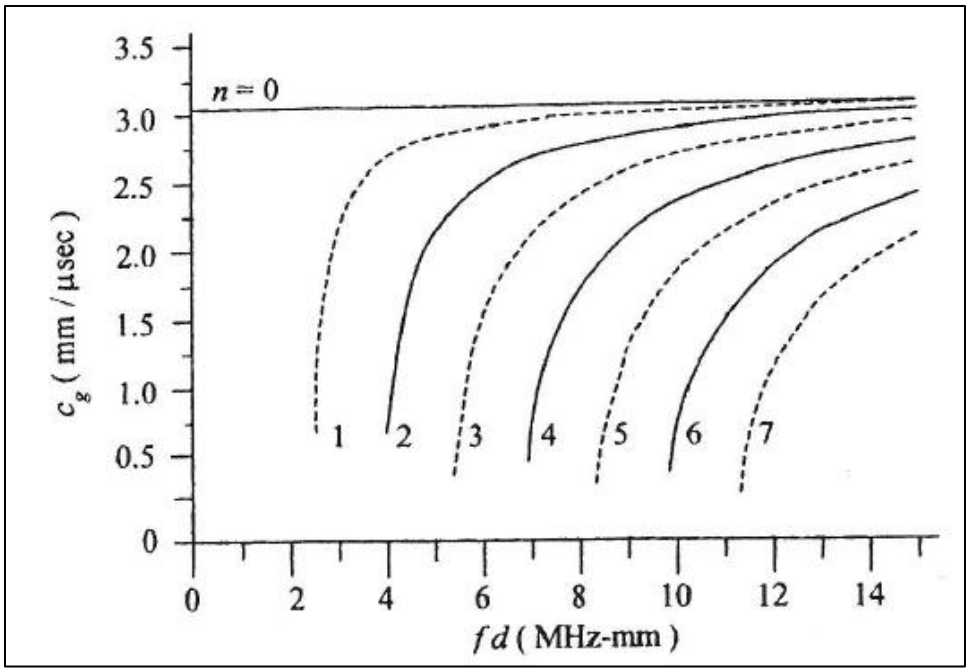

Figure 2.3. SH mode phase velocity dispersion curves for an aluminum layer: solid curves denote symmetric modes: dashed curves denote antisymmetric modes (Rose, 1999)

2.4.2 Group Velocity of Shear Horizontal mode

The dispersion equation provided in equation 2.3, can be used to determine the mathematical expression for the group velocity of any given SH mode. Taking the differential of both sides of the dispersion equation (right hand side is a constant for any *n*), the result is

$$\frac{2\omega d\omega}{{c_T}^2} - 2kdk = 0 \tag{2.6}$$

Solving this equation for dω/dk (by definition, the group velocity) yields

$$\frac{d\omega}{dk} = \frac{k{c_T}^2}{\omega^2} \tag{2.7}$$

Solving equation 2.3 for *k*, substituting the result into equation 2.7, and simplifying, yields the group velocity c_g of any SH mode which is shown in equation 2.8 below.

$$c_g(fd) = c_T \sqrt{1 - \frac{\left(n/2\right)^2}{\left(fd/c_T\right)^2}} \qquad (fd \geq (fd)_n) \tag{2.8}$$

From this equation 2.8, it can be seen that at the cutoff frequencies given by equation 2.5, the group velocity of any mode is zero. As *fd* approaches infinity for any given fixed *n*, the group velocity of any SH mode approaches bulk shear waves c_T (Zhang, Schulz, Naser, Ferguson, & Pai, 1999). Figure 2.4 shows the SH mode group velocity curves for the first eight SH modes in an aluminum layer with shear wave speed c_T = 3.1 mm/μs. The solid curves denote symmetric modes while the dashed curves represent antisymmetric modes.

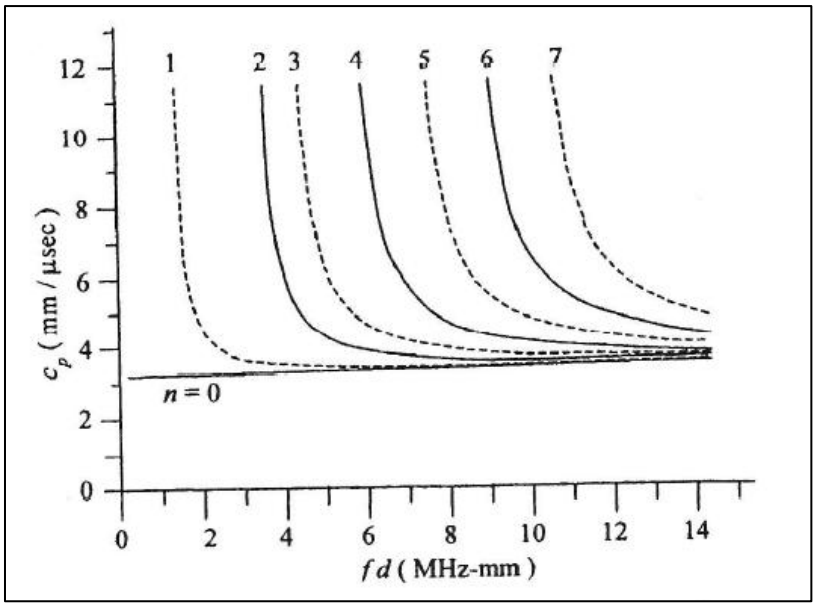

Figure 2.4. SH mode group velocity dispersion curves for the aluminum layer (Rose, 1999)

2.4.3 Excitation of Shear Horizontal Modes in Flat Layers

Viktorov (1967) presented the wedge technique to excite shear horizontal guided waves in isotropic layers. Using the spatial Fourier transforms, the excitability functions of the SH modes can be obtained from the results. SH modes are a synthesis of pure out of plane shear waves, the tractions applied to the surface of the layer must also have an out of plane shear component, which can only be achieved by using a viscous couplant (e.g., honey or silicone) between the wedge and layer (Viktorov, 1967). Additionally, a shear wave transducer must be used as the sending and receiving elements.

2.5 Piezoelectric Ceramics

Piezoelectric ceramics are hard, chemically inert and completely insensitive to humidity or other atmospheric influences. Their mechanical properties resemble those of the better known ceramic insulators and they are manufactured by much the same processes (Cady, 1964). Piezoelectric components are ideal for electromechanical transducers. Some examples of the many applications you will find piezoelectric ceramics used in, are given below.

Generators (conversion of mechanical into electrical energy)

- Spark igniters
- Solid-state batteries

Sensors (conversion of mechanical force or movement into a (proportional) electric signal)

- Acceleration sensor

- Pressure sensor
- Knock sensor (internal-combustion engines)

The piezoelectric effect was discovered by Jacques and Pierre Curie in 1880 (Cuc, Giurgiutiu, Joshi, & Tidwell, 2007). They found that if certain crystals were subjected to mechanical strain, they became electrically polarized and the degree of polarization was proportional to the applied strain. These same materials however deforms when they are exposed to an electric field. This phenomenon has become known as the inverse piezoelectric effect. The piezoelectric effect is exhibited by a number of naturally occurring crystals, for example quartz and sodium potassium tartrate (Waanders, 1991). For a crystal to exhibit the piezoelectric effect, its structure should have no center of symmetry.

A compressive or tensile stress applied to such a crystal will alter the separation between the positive and negative charge sites in each elementary cell leading to a net polarization at the crystal surface (Mason, 1960). Above the Curie point temperature, these crystallites exhibit simple cubic symmetry, the elementary cell of which is shown in Figure 2.5(a). This structure which is centrosymmetric has no dipoles present in the material because the positive and negative charge site coincides. However, below the curie point, the crystallites take on tetragonal symmetry in which the positive and negative charge sites no longer coincide (Figure 2.5(b)), so each elementary cell then has a built in electric dipole which may be reversed and also switched to certain allowed directions by the application of an electric field.

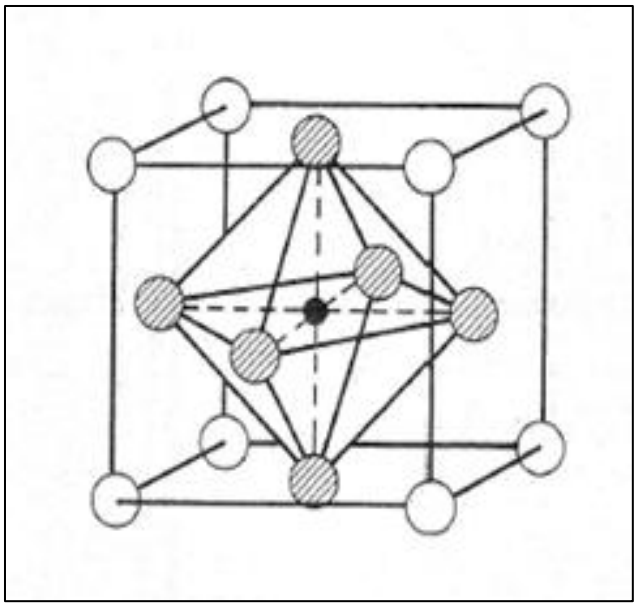

(a)

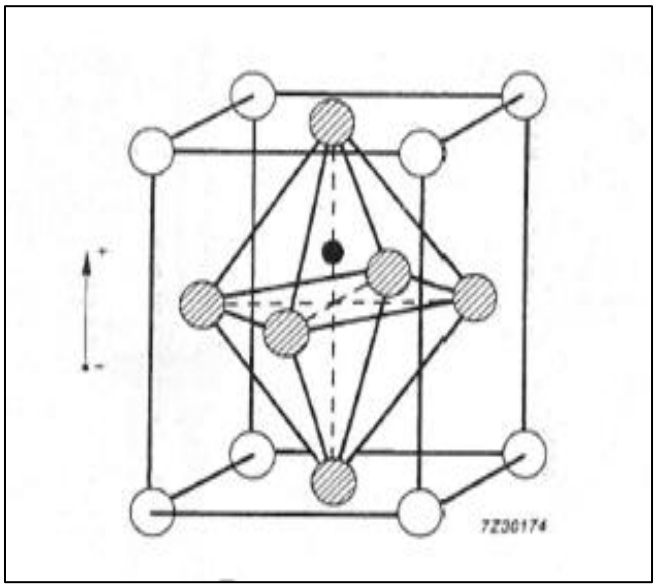

(b)

Figure 2.5. Piezoxide elementary cell. (a) cubic lattice (above Curie temperature); (b) tetragonal lattice (below Cure temperature) (Waanders, 1991)

The dipoles in a piezoelectric material are not randomly oriented throughout the material. Neighboring dipoles align with each other to form regions of local alignment known as Weiss domains. Within a Weiss domain, therefore, all the dipoles are aligned, giving a net dipole moment to the domain, and hence a net polarization (dipole moment per unit volume).

The direction of polarization between neighboring Weiss domains within a crystallite can differ by 90° or 180° and owing to the random distribution of Weiss domains throughout the material (Figure 2.6(a)), no overall piezoelectric effect is exhibited. The ceramic may be made piezoelectric in any chosen direction by a poling treatment which involves exposing it to a strong electric field at a temperature slightly below the Curie point (Figure 2.6(b)).

Under the action of this field, domains most nearly aligned with the field will grow at the expense of other domains. The material will also lengthen in the direction of the field. When the field is removed (Figure 2.6(c)), the dipoles remain locked in approximate alignment, giving the ceramic material a remanent polarization and a permanent deformation (i.e., making it anisotropic). The poling treatment is usually the final treatment of piezoxide component manufacture.

If an initially unpolarized sample of piezoxide is subjected to an increasing electric field at a temperature slightly below its Curie point, the dipoles become increasing aligned with the field and the polarization will follow the initial curve. When the field has increased beyond a certain value, no further increase in polarization will be observed because the dipoles are then all aligned with the field.

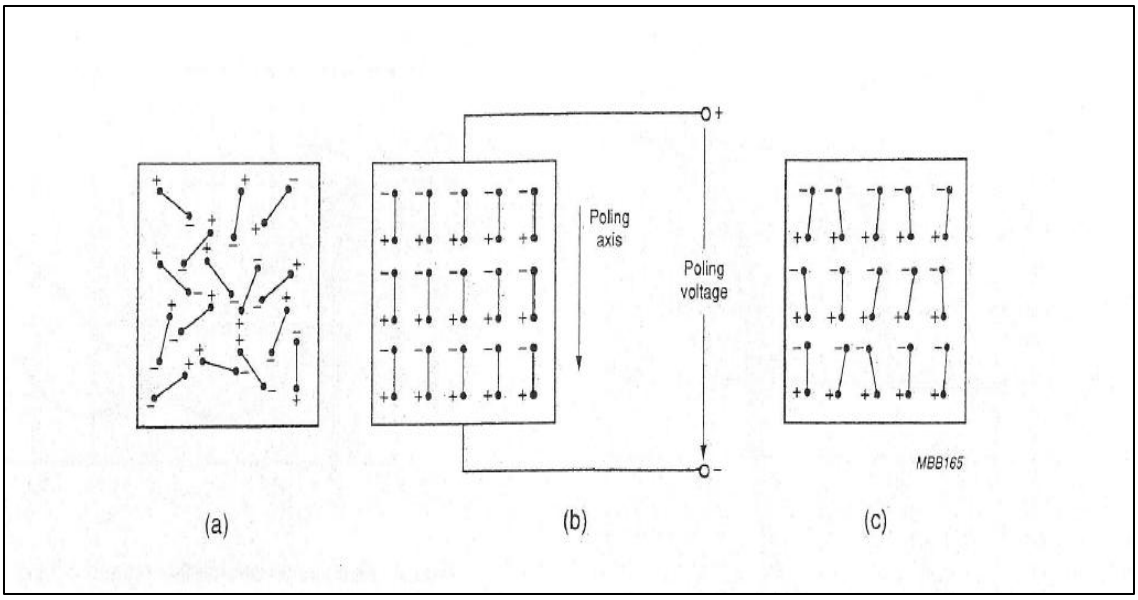

Figure 2.6. Electric dipole moments in Weiss domains. (a) before polarization; (b) during polarization; (c) after polarization (Waanders, 1991)

2.6 Bonding Techniques of Piezoelectric Ceramics

Cook and Jaffe (1971) discussed three principal methods to bond piezoelectric ceramics to some substrate, which are clamping, gluing and soldering. Clamping is often unreliable as the function of the piezoxide (PXE) element is to move and so clamping limits the purpose of this element (Jaffe, Cook, & Jaffe, 1971). Soldering has the advantage of giving a strong conductive connection however, the displacement of the PXE causes fatigue in the soldering bond. Gluing is usually considered the best approach. Modern epoxy- or acrylate glues, in particular provide strong yet still flexible joints between adjacent surfaces. Also, there is no fatigue and operating temperatures up to 150 °C are no problem for some of the glues.

Mason (1960) stated that, electrical contact between the substrate and the electrode on the PXE is nearly always required. Conductive glue is one possibility,

however, they are heavily loaded with conductive particles that the glue line is often weak. Also, conductive glue has a three dimensional conductivity which can lead to short circuits. Another method is to roughen the surfaces to be glued. If the glue is cured under a pressure of 10^5 Pa, many point contacts between the surfaces will be formed, however, this method is not very reproducible. A better solution is to mix nickel powder with a well-defined particle size of approximately 10µm into the glue and applying even pressure during curing. Since nickel particles are almost ideal spheres they tend to form a monolayer between the surfaces ergo provide better electrical contact.

CHAPTER 3

EXPERIMENTAL RESULTS OF SHEAR WAVES

3.1 Introduction

It is possible to simulate acoustic emission wave generation and propagation experimentally through alternative means. Simulated acoustic emission signals are generated by means of applying transverse impulse into the structure. While reproducing fatigue crack growth at a desired location in a structure at will is difficult or impossible, the simulated AE events through such impulses can be applied readily on the surface of a structure and offers a convenient means of studying the complex wave propagation pattern in any structure. In this research, simulated AE signals are used to:

(1) Evaluate the sensitivity of the sensors in detecting shear horizontal AE signals

(2) Obtain an approximate measure of attenuation in the structure

(3) Examine how the waves propagate in the structure of the material

Traditionally, the longitudinal and vertical shear modes of wave propagation have been the most commonly used, because they are easily generated and detected. Horizontal shear waves however, more difficult to be generated and detected. In this study, piezoelectric transducers are used to obtain the horizontal shear.

Ultrasonic pulser or pencil lead break can be used to generate AE signals within the material (Dunegan, August 2000). In this research, the ultrasonic DECI pulser was used to replicate crack like signals as it is difficult to repeat the same type of signal with pencil lead break. As shown in Figure 3.1 and Figure 3.2, DECI model 600 pulser with

the SE 25-P transducer and a vice to hold the transducer in place for in plane excitation, was used. The DECI model 600 pulser is composed of a power cell and pulser while the SE 25-P transducer (Figure 3.2) is connected to the pulser with a cable. A metric ruler was also placed beside the DECI pulser to show the relative size of the equipment used.

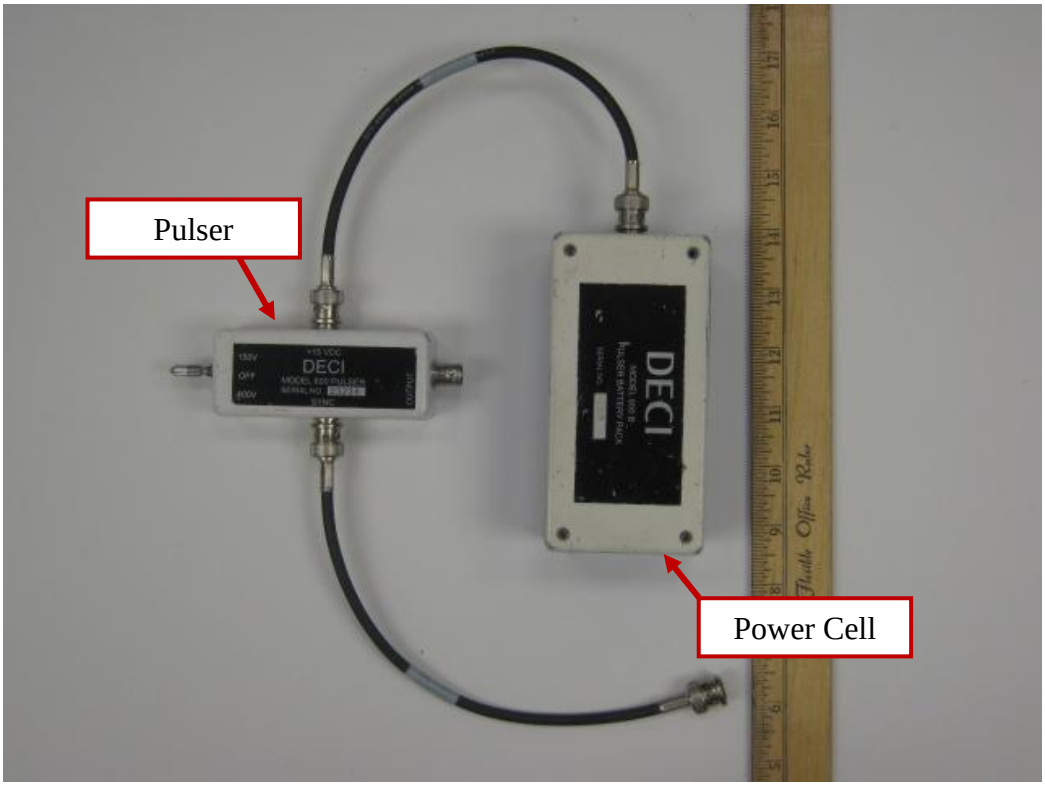

Figure 3.1. DECI model 600 pulser and battery

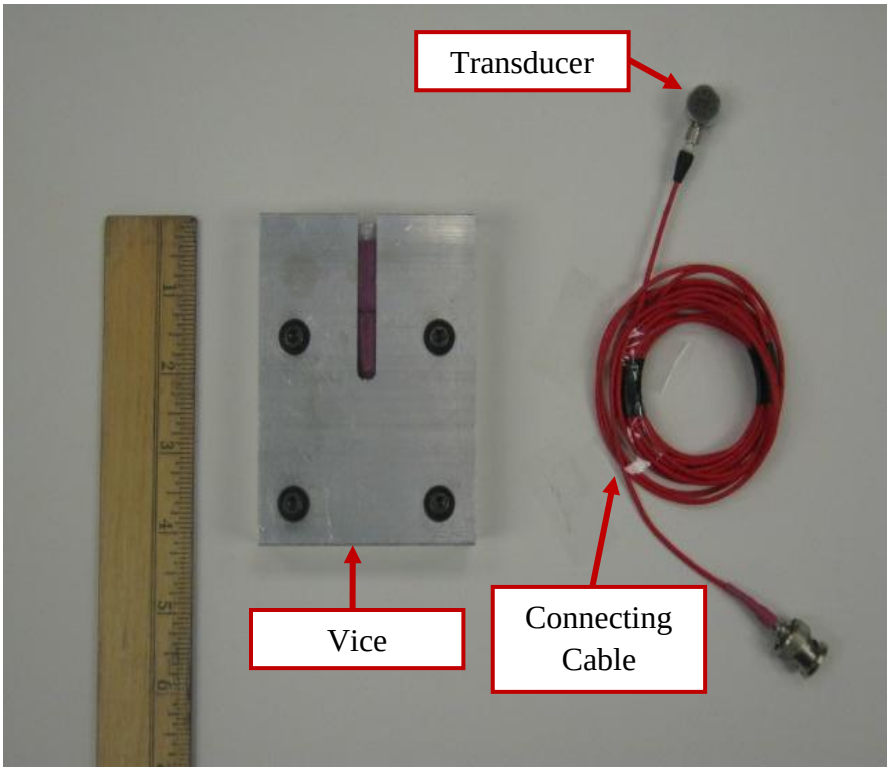

Figure 3.2. SE 25-P transducer and Vice for in plane excitation

3.2 Sensor Fabrication and Bonding

Fabrication of the sensor strip arrays starts with etching away the nickel electrode coating on both ends of the top surface of the 10 mm × 20 mm piezoelectric wafers, leaving a 3 mm × 2 mm electrical contact in the center. A copper shim stock was then glued with Loctite superglue across the electrical contacts on the piezoelectric wafers. The next step was to carefully cut the piezoelectric wafers into 10 mm × 2 mm strips. Five of these strips were then arranged parallel to one another with a spacing of 1 mm, with their center points passing through a 45° line as shown in Figure 3.3(a). A photograph of the actual shear sensor array prior to transfer and bonding to a specimen is shown in Figure 3.3(b).

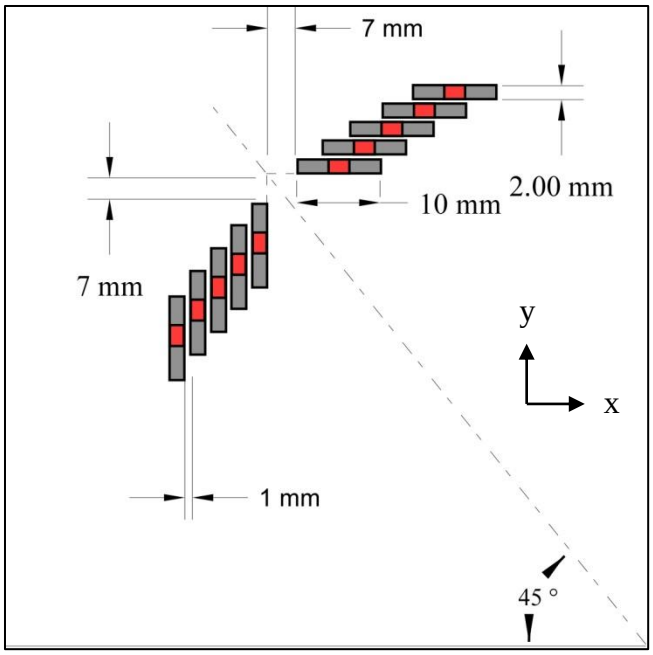

(a)

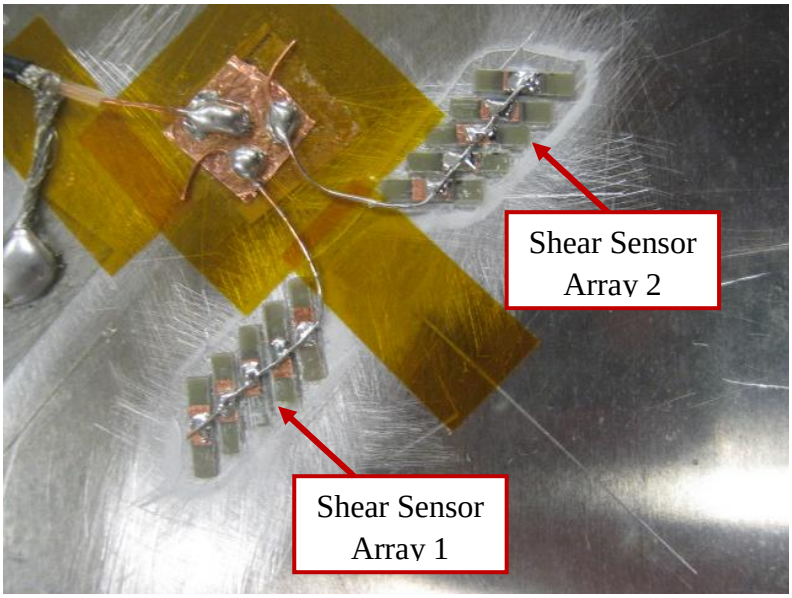

(b)

Figure 3.3. (a) Diagram of the piezoelectric shear senor array arrangement (b) photograph of the arranged shear sensor prior to transfer and bonding to a specimen

This array was then transferred with a piece of tape to the specimen site which had been roughened with sandpaper before being thoroughly cleaned and dried with acetone. A thin layer of Loctite superglue was spread over the location and the sensor array was held in place until the adhesive was cured. Care was taken to minimize any adhesive welling up into the gaps between individual strips so that the strips would act as individual strips, independent of stresses experience by adjacent strips in the array. A copper shim stock was then taped down across the electrical contacts on the strips and Kapton tape was used to insulate around the sensor array. It is important to note that shear sensor array 1 and 2 in Figure 3.3 are polarized in different directions (i.e. The upward face electrode of shear sensor array 1 was glued to the aluminum surface while the downward face electrode of shear sensor array 2 was glued to the aluminum surface).

3.3 Simulated Crack Acoustic Emissions with a Pulser

Prior to testing the ability of the shear sensor array to detect acoustic emissions from fatigue induced crack propagation, the sensor array was tested with simulated emissions generated by a piezoelectric pulser. The goal of these initial experiments was to establish the sensitivity of the sensor array to stress waves arriving at various angles and distances. The sensor array was bonded to an aluminum panel as noted above, and electrical leads were connected to the copper shim stock and the aluminum plate to measure the electrical signals generated by the arrival of the acoustic emission wave packets. The sensor was located 110 mm from the edge of the aluminum plate as shown in Figure 3.4. Signals were recorded corresponding to pulser locations spaced 10 mm on

either side of the 45 degree line shown in the figure. This arrangement was selected to represent a fatigue crack growing in a plate at a slow rate and understand the ability of the sensor to isolate the shear horizontal component of the acoustic emission signals under these conditions.

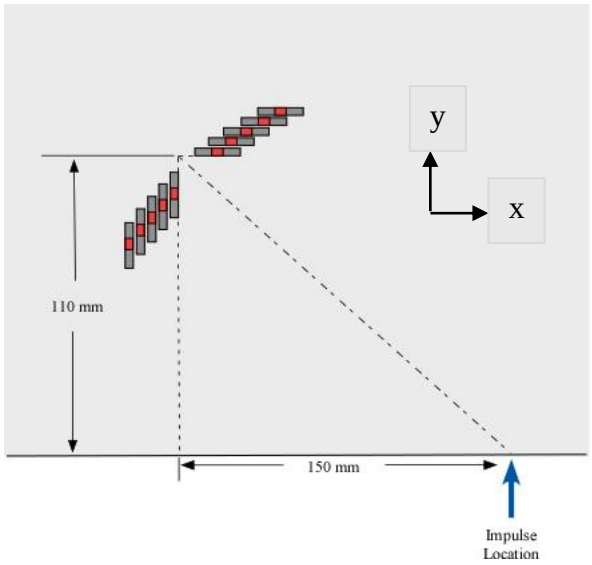

Figure 3.4. Diagram of the pulser placement along the edge and its relation to the distance and angle to the shear sensor array

This voltage output of the sensors was read by a LeCroy model LT344 oscilloscope when triggered by the synchronous output from the pulser. A vice was used to position the pulser along the edge of the specimen, which had been sanded, cleaned, and coated with Sonotech ultrasonic couplant, to ensure effective transmission of the impulse. The pulser excitation was set to 400V and the fixture ensured application of the impulse at the mid-plane of the specimen. The waveforms were filtered with a 20 MHz

bandwidth and averaged over 50 events before being saved for further analysis. Figure 3.5 below, shows the experimental setup of the simulated AE generated with a pulser.

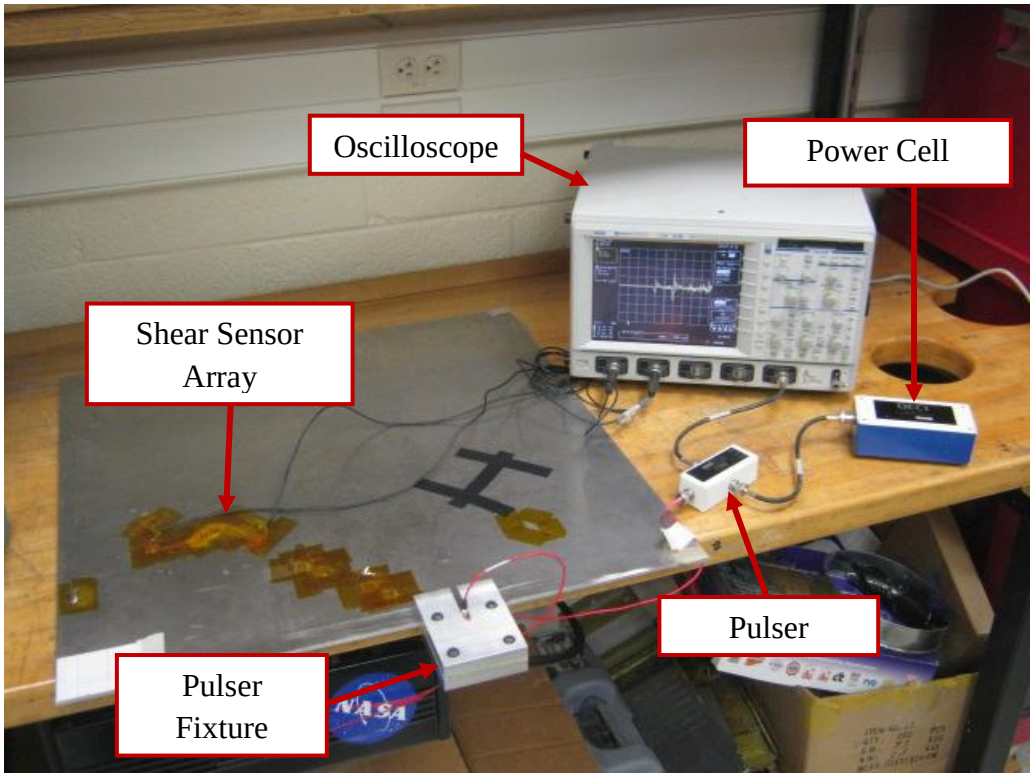

Figure 3.5. Experimental setup for the pulser simulated emissions

3.4 Fatigue Loading of the Aluminum Specimen

Following the pulser tests, testing shifted to detection of acoustic emissions resulting from fracture propagation. The experiments were carried out on a panel of 2024-T3 aluminum measuring 600 mm × 300 mm × 3 mm thick. A slot 1 mm wide and 62 mm long was cut at the midpoint of the long side and the end of this slot was sharpened to a point, producing a large stress concentration to promote crack growth. The estimated fracture toughness for a sharp crack at this location was determined to be 34

MPa√m based on linear elastic fracture mechanics considerations (Norman E. Dowling, 2007). The specimen with the end fixtures are clamped tightly into two hydraulic grips of the material test system (MTS), leaving the central 457 mm × 305 mm portion of the aluminum plate exposed. The specimen with the end fixtures are shown in Figure 3.6 below. The specimen was subjected to tensile loads cycling from 500 lbs. to 5500 lbs. with a frequency of 2.5 Hz for a total of 15000 cycles to produce a 5 mm crack extending from the sharpened point of the slot.

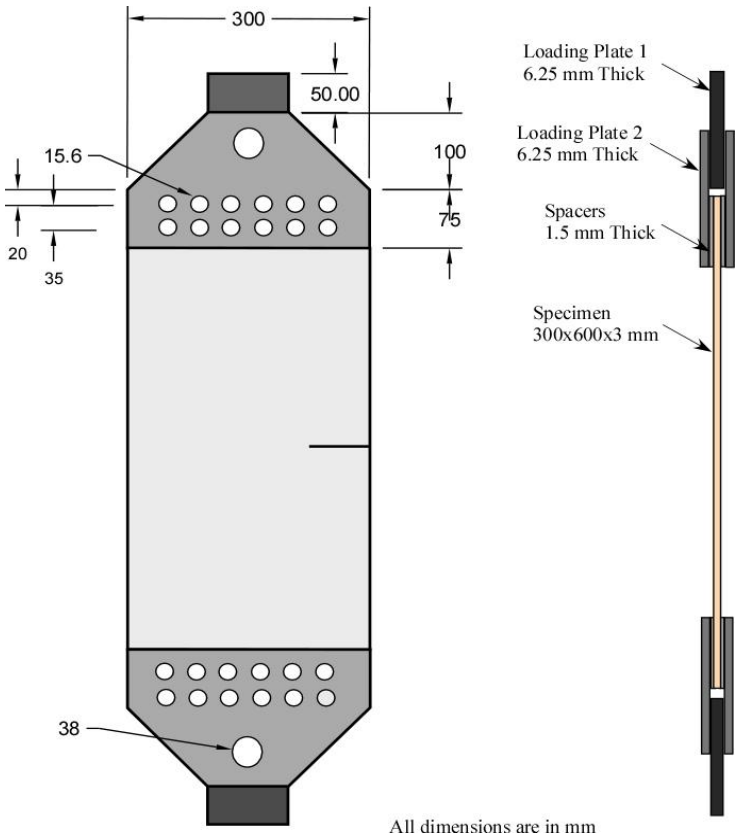

Figure 3.6. Specimen with end fixture used in the SHM experiments

The experimental setup used for the SHM tests is shown in Figure 3.7 below. The load applied on the specimen was preset in the MTS controller. AE sensor was connected to the data acquisition system through preamplifiers. This system recorded both the conventional acoustic emission parameters such as the acoustic emission amplitude, rise time, duration, etc. In addition, the system recorded the waveforms corresponding to each of the recorded acoustic emission signals.

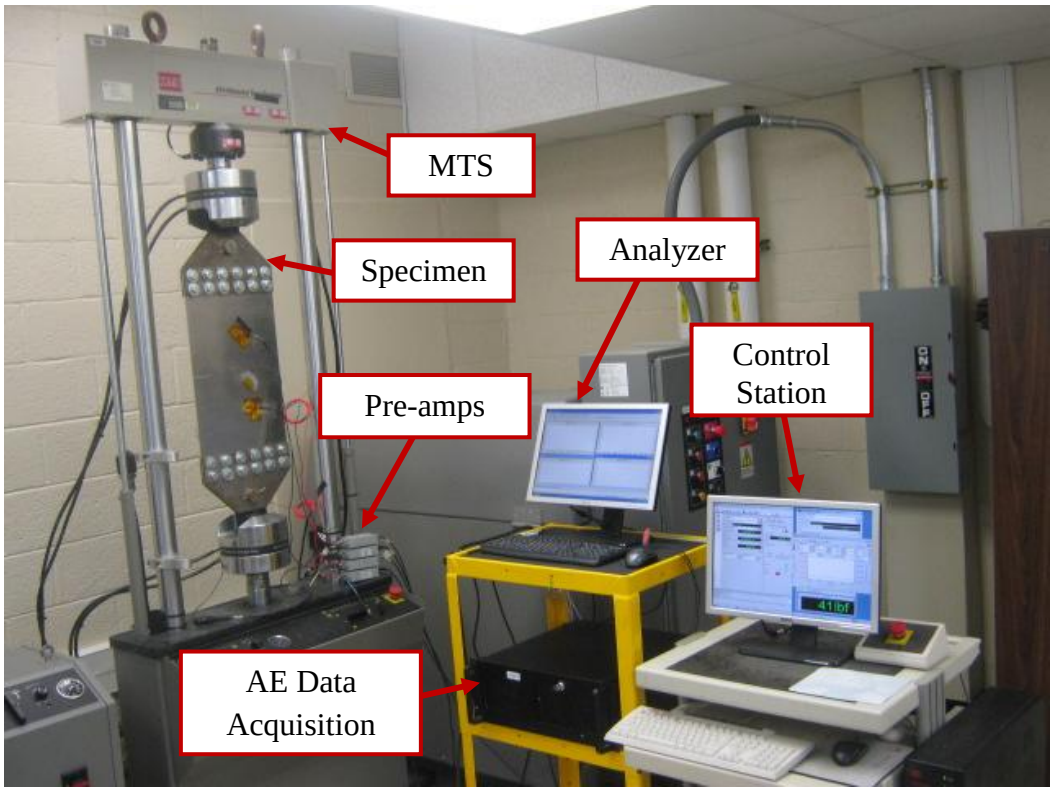

Figure 3.7. Test Setup for Monitoring the Crack Growth with Shear Sensor Array on Aluminum Plate Specimen

Table 3.1 lists the instrument settings including the threshold level for each channel, the preamplifier gain and the pre-trigger which is the time before which the waveform passes the threshold. Slightly higher threshold levels were required for the bonded sensors because of their wide band frequency response which resulted in greater sensitivity to noise signals.

Table 3.1. Acoustic emission instrument settings

Channel	Threshold (dB)	Preamplifier Gain (dB)	Pre-Trigger (μs)
1	35	40	256
2	35	40	256
3	40	40	256
4	35	40	256

The performance and sensitivity of all four sensors were verified prior to the acquisition of crack related AE signals using in-situ lead break test. The lead break was located at the notch tip. The resulting waveforms from the bonded wafer sensors are shown in Figure 3.8(a) and Figure 3.8(c), while the resulting waveforms from the resonant frequency sensors are shown in Figure 3.8(b) and Figure 3.8(d). Amplified signals were recorded using the AE data acquisition system with sampling rate of 5 million samples per second. Evidence of the shear horizontal component is observed in Figure 3.8(a) and Figure 3.8(c) at 300 μs with high voltage amplitude of 2 V.

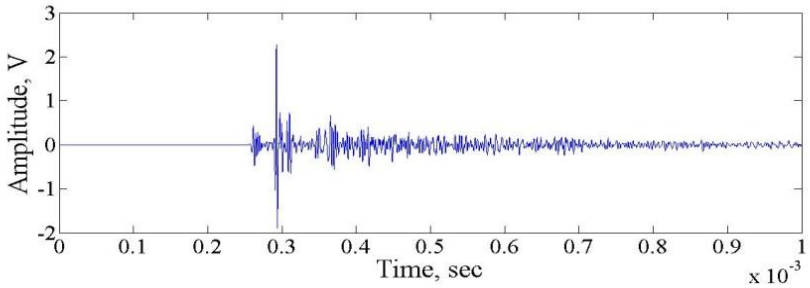

(a)

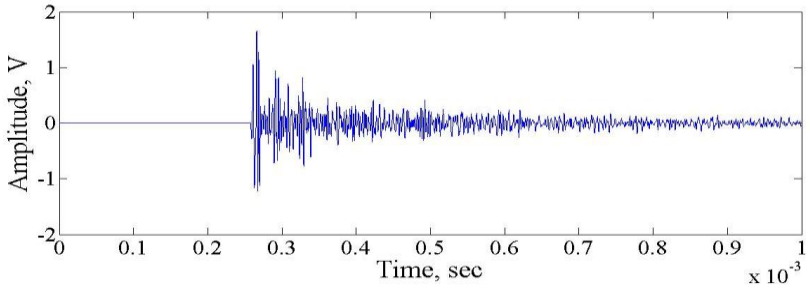

(b)

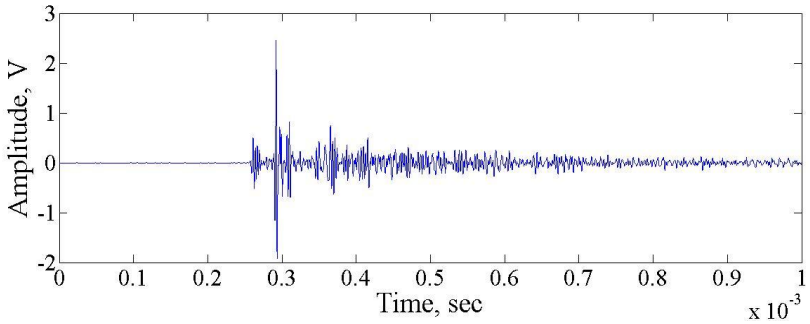

(c)

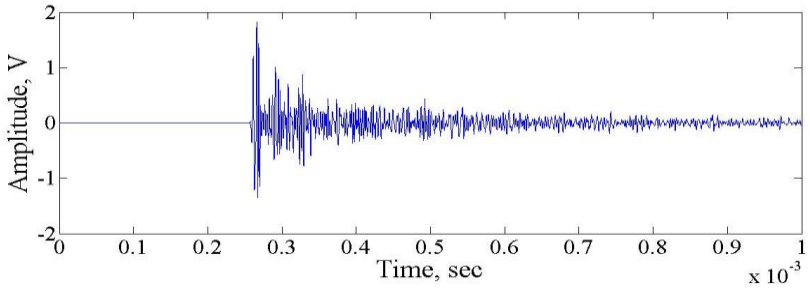

(d)

Figure 3.8. AE waveform signals using in-situ lead break test, (a) and (c) shear sensor array while (b) and (d) bonded piezoelectric wafer

The layout of the various sensors on the front and back side of the specimen can be seen in Figure 3.9(a) and Figure 3.9(b) below. The location chosen for the strip sensor array was at a radial distance of 150 mm from the crack tip along a line inclined at a 45° to the expected direction of travel.

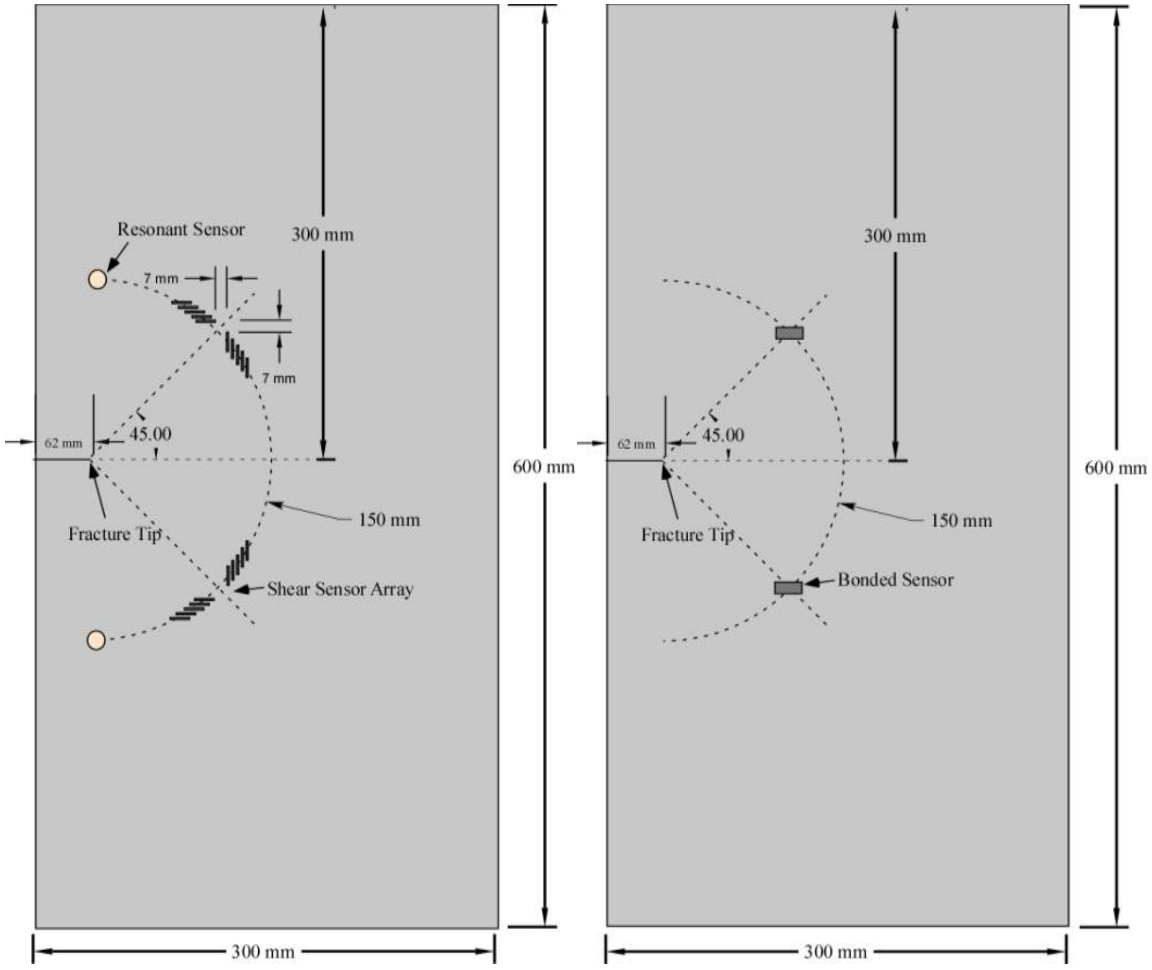

(a) (b)

Figure 3.9. Sensor layout for the fatigue crack propagation tests, (a) front side view (b) back side view

A conventional PZT sensor was bonded to the specimen at the same location as the shear sensors, but on the back surface (Figure 3.9 (b)). The copper leads from the top of each of these sensors was soldered to the core of a coaxial cable, with the outer strands soldered to copper pads bonded to the sample as grounds. Two R30 resonance based sensors from Physical Acoustics Corporation were attached to the specimen on opposite sides the fracture. The timestamps from two sensors were compared to those of the bonded sensor and shear sensor array to validate that the measured signals were originating from the crack tip.

The specimen was subject to tensile loads cycling from 2.5 kips to 6 kips with a frequency of 1 Hz. The sensors were connected to the AE monitor through preamplifiers set a gain of 40 dB. The threshold for data acquisition was set at 35 dB. The waveforms were collected at 5 million samples/s for 5000 samples, giving a 1 ms duration of recording for each AE signal. The time of arrival of signals at the shear sensor array and bonded sensor were then manually screened to validate that they are from the fatigue cracks and not from extraneous sources. This was facilitated by the arrival times for signals recorded by resonant sensors placed on either side of the crack.

3.5 Experimental Results

The waveforms in Figure 3.10 (a) along with its corresponding wavelet analysis Figure 3.10(b), collected from the pulser experiments at 30 degrees, revealed evidence of the shear wave as shown below. As was expected, the shear component was small when the distance to the pulser was the greatest and the angle of approach was small (Figure

3.10(a)). The different velocities of the various modes is also evident in Figure 3.10(a), where the greater distance has allowed more time for the peaks of the S_0 and shear mode to separate compared to the shorter distance of Figure 3.11(a). Hence it can be summarized that between 30 and 45 degrees, the shear horizontal component is evident but as the angle of incidence approaches beyond 45 degrees the shear horizontal component subsides or becomes nonexistent.

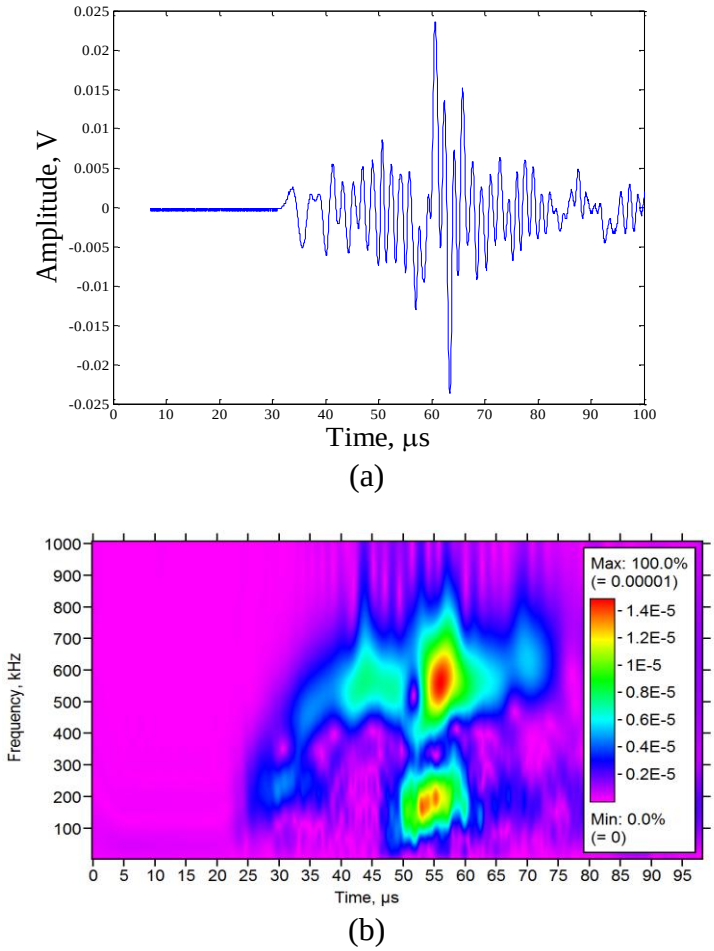

(a)

(b)

Figure 3.10. (a) Acoustic emission waveforms from shear sensor pulser tests at 30 degrees (b) wavelet analysis of acoustic waveform at 30 degrees

Figure 3.11 (a) shows that the distance between the S_0 peak and the SH_0 peak shortens with closer proximity to the pulser and as the angle approached 45°. Also from the same Figure 3.11 (a), it can be observed that when the sensor is located at the angle of 45 degrees to assumed crack plane, maximum shear horizontal component is detected. From the corresponding wavelet analysis (Figure 3.11(b)) of the AE signals, maximum amplitude of the horizontal component occurs at around 200 kHz.

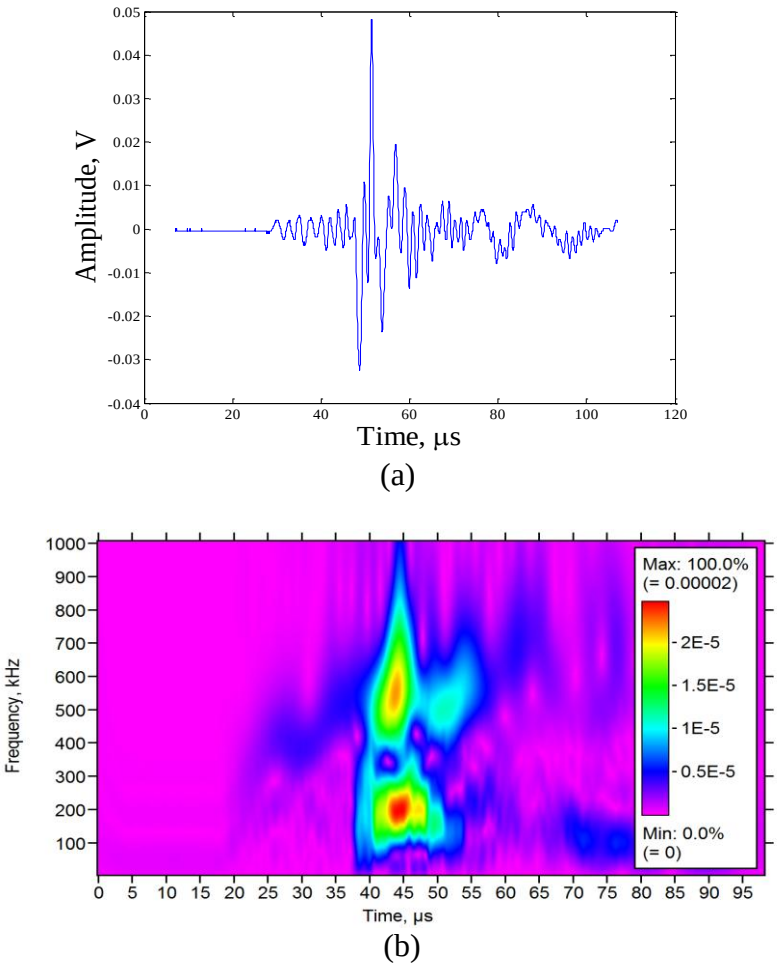

(a)

(b)

Figure 3.11. (a) Acoustic emission waveforms from shear sensor pulser tests at 45 degrees (b) wavelet analysis of acoustic waveform at 45 degree

The waveforms in Figure 3.12 (a) along with its corresponding wavelet analysis Figure 3.12(b), collected from the pulser experiments at 60 degrees, did not revealed strong evidence of the SH component. This is because the fraction of the shear component energy of the acoustic emission signal is located at 45 degrees from the incoming acoustic emission.

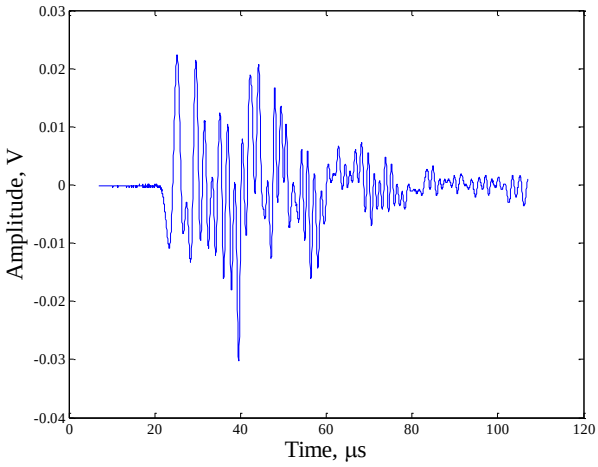

(a)

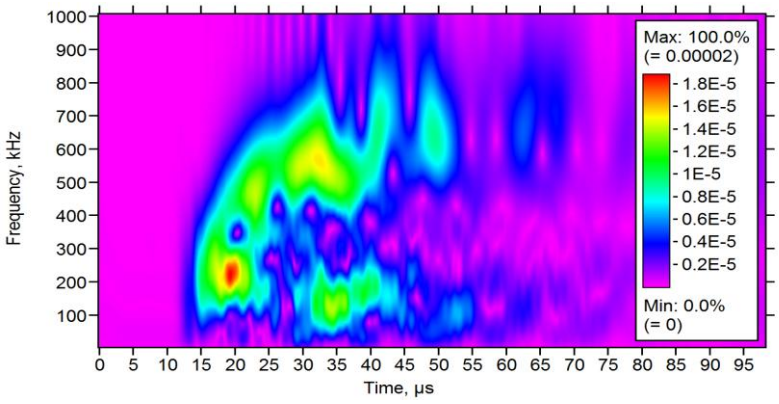

(b)

Figure 3.12. (a) Acoustic emission waveforms from shear sensor pulser tests at 60 degrees (b) wavelet analysis of acoustic waveform at 60 degrees

In Figure 3.13(a) below, the shear component of the acoustic emission waveform is not detected by the shear sensor at 90 degrees. Only the S_0 component is evident which occurred at approximately 20 μs. It is to be noted that at 90 degrees, only one of the shear sensor would receive a larger percentage of the incoming acoustic emission wave signals. From the corresponding wavelet analysis (Figure 3.13(b)) of the AE signals, maximum amplitude of the antisymmetrical component occurs at around 600 kHz.

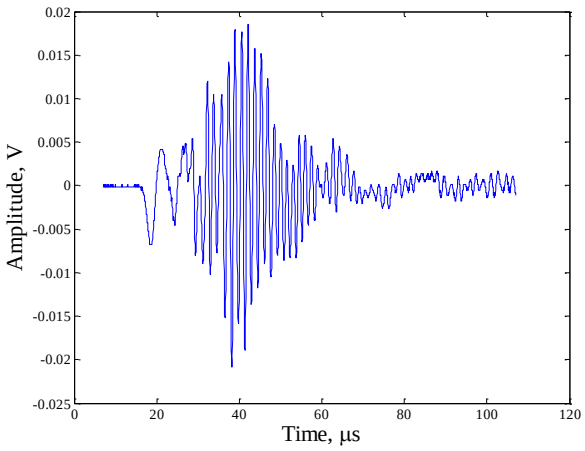

(a)

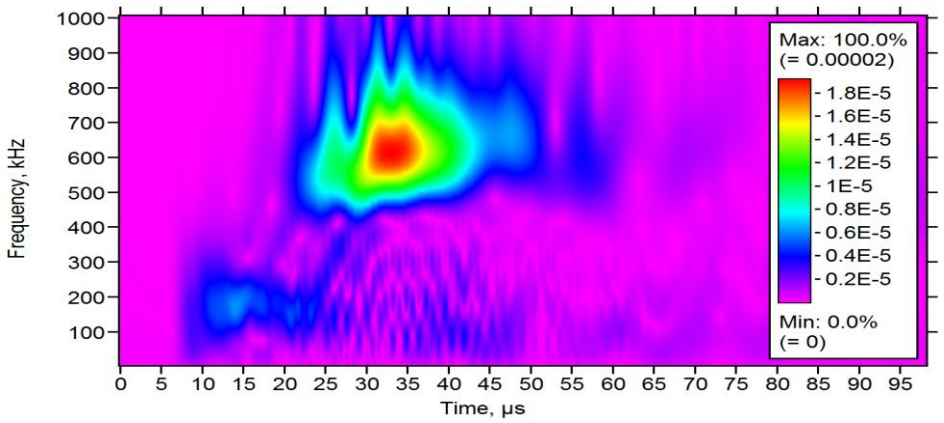

(b)

Figure 3.13. (a) Acoustic emission waveforms from shear sensor pulser tests at 90 degrees (b) wavelet analysis of acoustic waveform at 90 degrees

AGU-Vallen Wavelet analysis program was used for obtaining the wavelet analysis shown. A time-frequency transform distributes the energy of a wave in time and frequency. Hence, it is possible to identify the time of arrival of different frequency components. To obtain only the shear horizontal component of the waveform from both the finite element and the actual experiment, the shear sensor waveform along the x-direction were obtained separately from the shear sensor waveform along the y-direction and added together. Theoretically, the S_0 component from both sensors should be equal and opposite in direction, so when both waveforms are added together, the S_0 component cancels.

However, in this experiment, it is observed that the S_0 component is not completely cancelled. Figure 3.14(a) shows the waveform of shear sensor along the x direction, Figure 3.14(b) shows the waveform of shear sensor along the y direction and the shear waveform from the combination of the two shear sensor waveforms is shown in Figure 3.14(c). The S_0 amplitude was not sufficiently cancelled because the two different shear sensor arrays may not be perfectly electrically balanced due to normal wear and tear of the solder electrical connections. Also, after certain number of fatigue cycles, the bonding between the piezoelectric strip sensor and the aluminum specimen may weaken. Thus decreasing the necessary contact needed to obtain high amplitude acoustic emission signals.

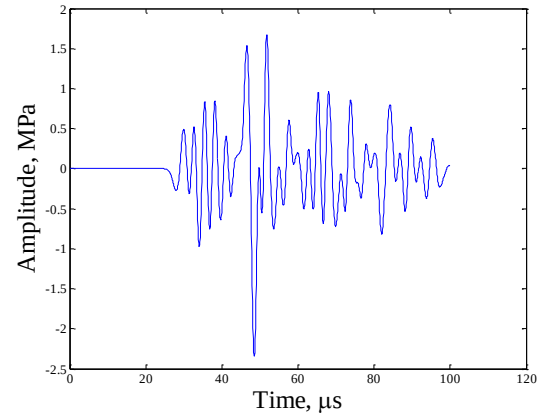

(a)

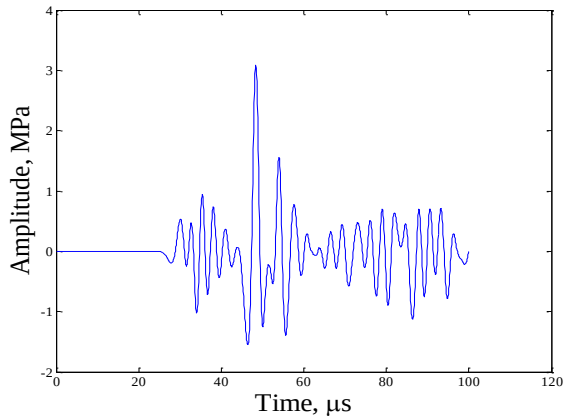

(b)

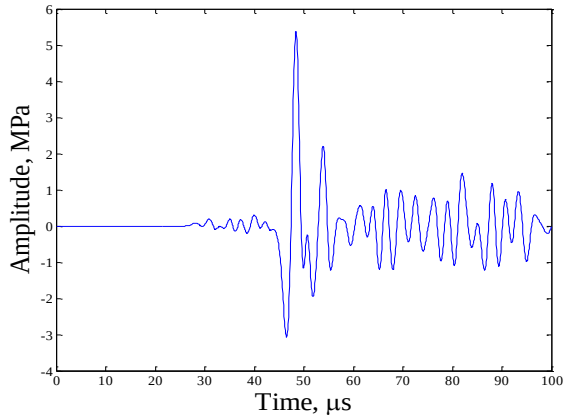

(c)

Figure 3.14. Illustration of the shear component from the shear sensor arrays (a) shear sensor along the x axis (b) shear sensor along the y axis (c) difference in waveform from both shear sensors

Verification of the shear sensor array to produce repeatable shear horizontal waveforms were determined by plotting five consecutive waveforms obtained during fatigue crack growth after their amplitudes were normalized to span the range of -1.0 V to +1.0 V, so that they can easily be compared. To obtain this normalize amplitude, all voltage data points in each of waveforms was divided by the highest voltage value in the waveform. The five normalized waveforms were superposed in Figure 3.15 below. The figure shows that the actual shear wave components in AE signals corresponding to close sequence of crack growth events are nearly identical.

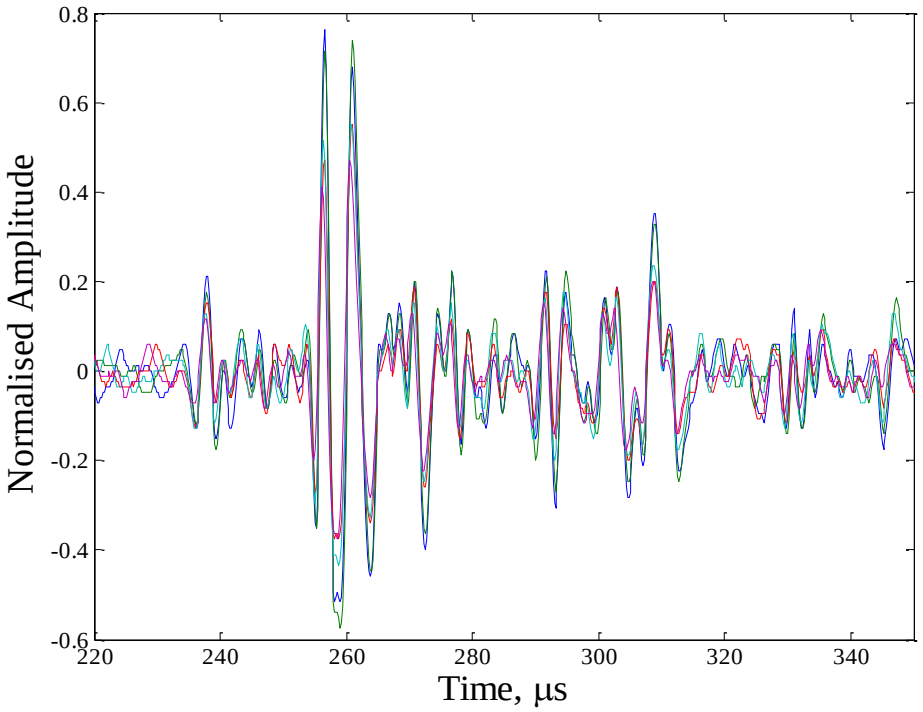

Figure 3.15. Normalized amplitude plot of the first five consecutive shear waveforms

Waveform from the wafer sensor, shear sensor array, finite element model of shear sensor and resonant sensor output, were compared to identify the shear horizontal component of the crack growth related acoustic emission signals. It is well known that incremental crack growth over a microscopic area located at the neutral axis leads to predominantly S_0 mode in the waveform and similar crack growth located far from the neutral axis leads to predominantly A_0 mode in the waveform. These details are observable in bonded wafer sensor because of its wide band sensitivity while not evident in resonant frequency sensors.

Hence to identify the proximity of incremental crack growth to the neutral axis, the ratio of peak values of the A_0 component to the S_0 component was determined from the PZT waveform sensor. If the incremental crack growth is close in proximity to the neutral axis, then the ratio of peak values of the A_0 component to the S_0 component should be generally less than one. However, if the incremental crack growth is near in proximity to the surface edge, the ratio of A_0 component to S_0 component should be in general greater than one. In the waveforms resulting from fatigue crack growth, the ratio of A_0 to S_0 ranged from 0.4 to 8.5. Figure 3.16(a) and Figure 3.16(b) compares acoustic emission waveform with its wavelet analysis of the same event from the resonant sensor, where the crack growth appears to be propagating at or near the neutral axis, as the ratio between A_0 to S_0 from the PZT waveform sensor was 0.45.

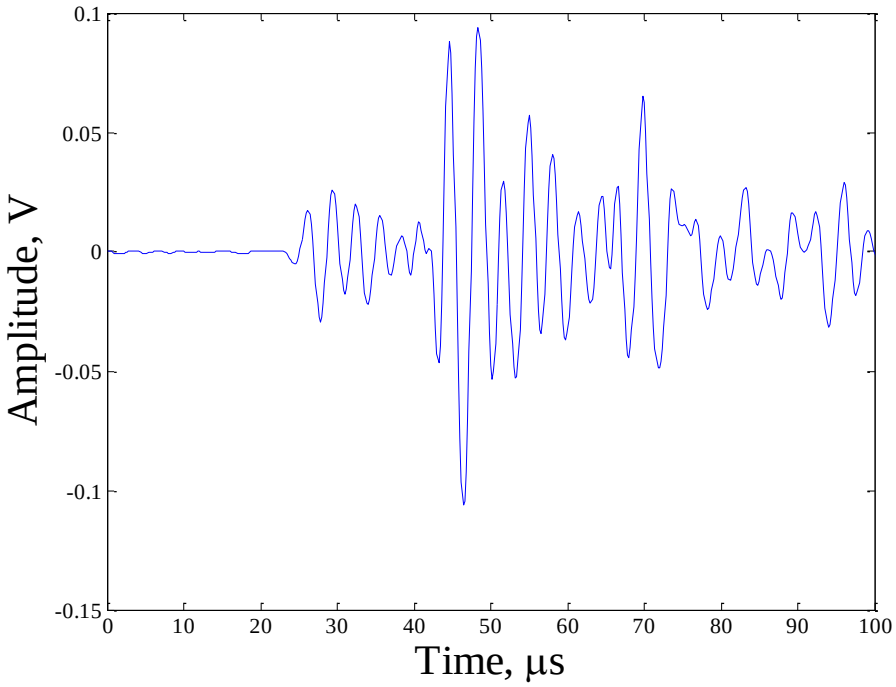

(a)

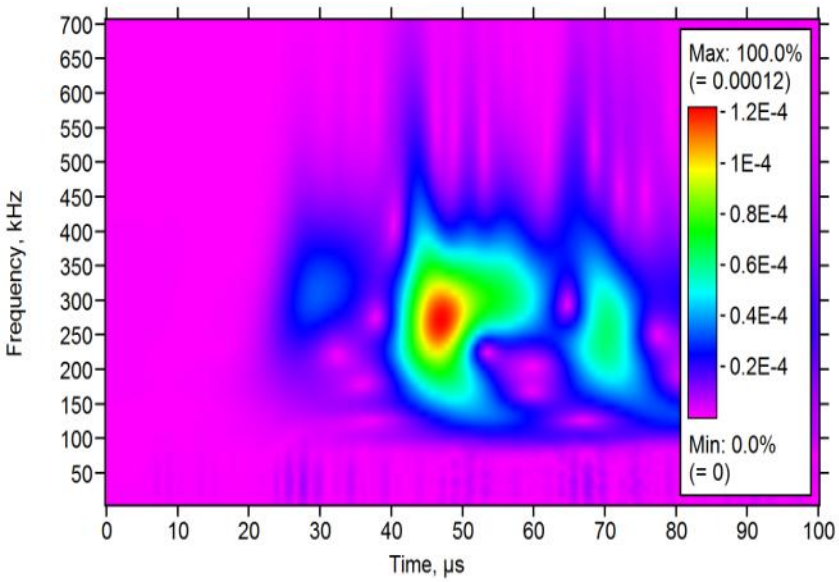

(b)

Figure 3.16. (a) Neutral axis crack growth signal from resonant sensor (b) wavelet analysis of the acoustic emission signal

Figure 3.17(a) and (b) shown below, compares acoustic emission waveform with its corresponding wavelet analysis of the same event from the shear sensor, where the crack growth appears to be propagating at or near the neutral axis, as the ratio between A_0 to S_0 from the PZT waveform sensor was 0.45. Figure 3.17(a) delineates a SH component of peak amplitude 0.06 V at around 45 µs at frequency approximately 200 kHz.

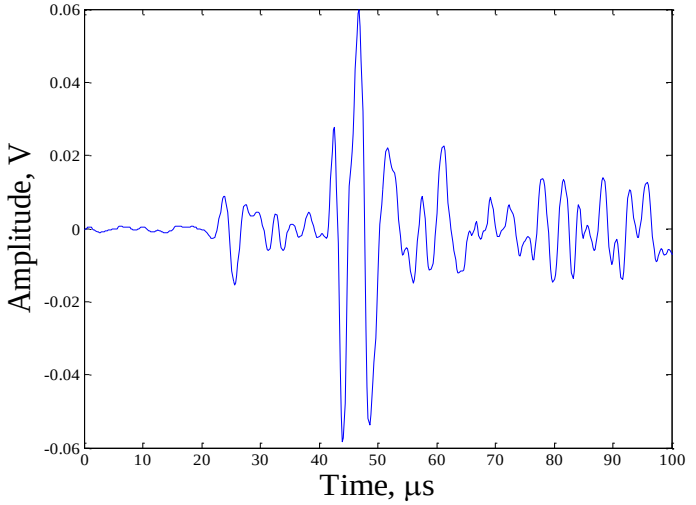

(a)

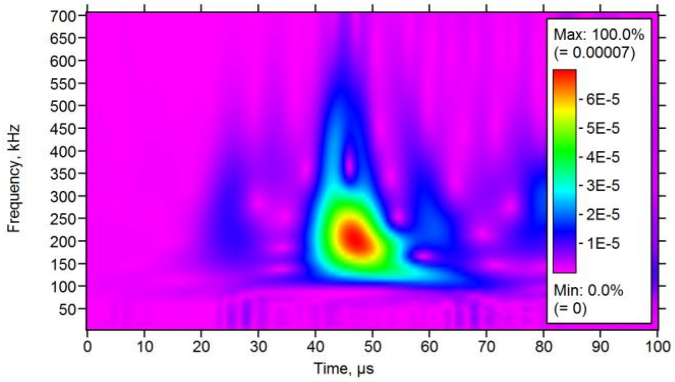

(b)

Figure 3.17. (a) Neutral axis crack growth signal from shear sensor (b) wavelet analysis of the acoustic emission signal

Figure 3.18(a) and (b) shown below, compares acoustic emission waveform with its wavelet analysis of the same event from the wafer sensor, where the crack growth appears to be propagating at or near the neutral axis, as the ratio between A_0 to S_0 from the PZT waveform sensor was 0.45. The acoustic waveform (Figure 3.18(a)) exhibits S_0 component of peak amplitude 0.15 V at 30 µs and A_0 component at approximately 50 µs.

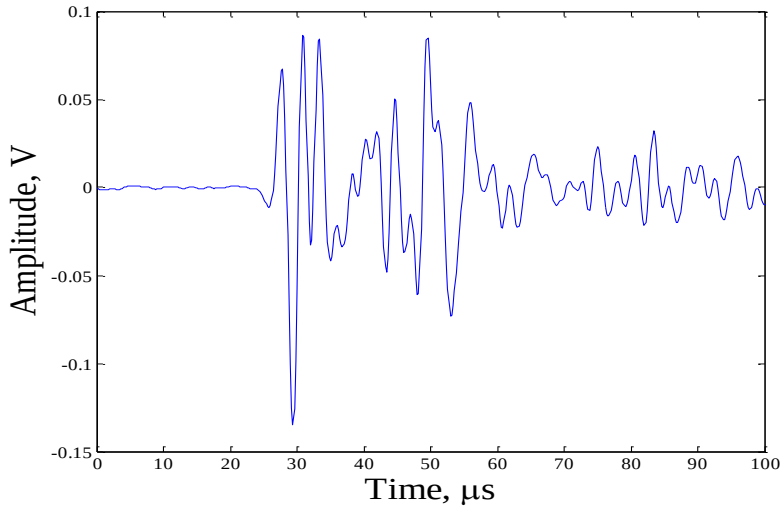

(a)

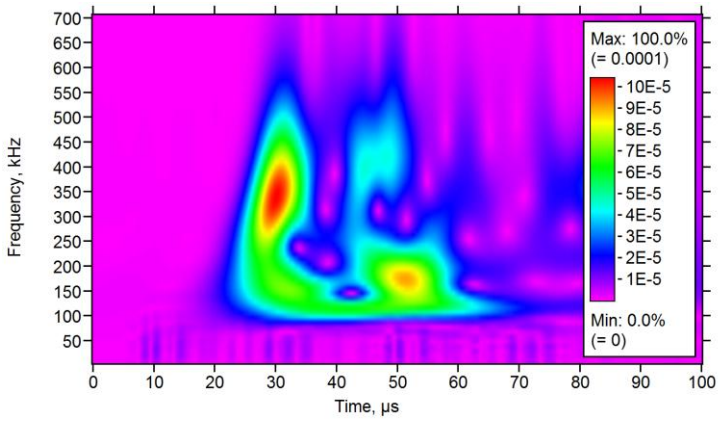

(b)

Figure 3.18. (a) Neutral axis crack growth signal from wafer sensor (b) wavelet analysis of the acoustic emission signal

Figure 3.19(a) shown below, compares acoustic emission waveform with wavelet analysis (Figure 3.19(b)) of the same event from the shear sensor, where the crack growth appears to be propagating at or near the surface, as the ratio between A_0 to S_0 from the PZT waveform sensor was 8.3.

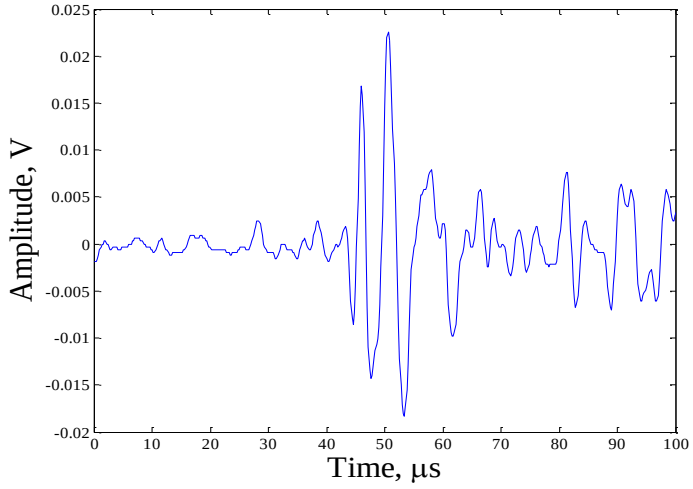

(a)

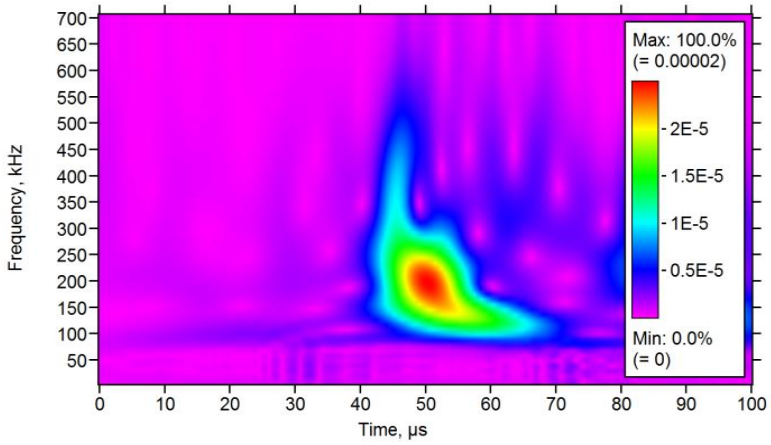

(b)

Figure 3.19. (a) Surface crack growth signal from shear sensor (b) wavelet analysis of the acoustic emission signal

Figure 3.20(a), compares acoustic emission waveform with its wavelet analysis (Figure 3.20(b)) of the same event from the wafer sensor, where the crack growth appears to be propagating at or near the surface. The acoustic waveform (Figure 3.20(a)) exhibits S_0 component of amplitude 0.008 V at 30 µs and A_0 component of peak amplitude 0.05 V at approximately 50 µs.

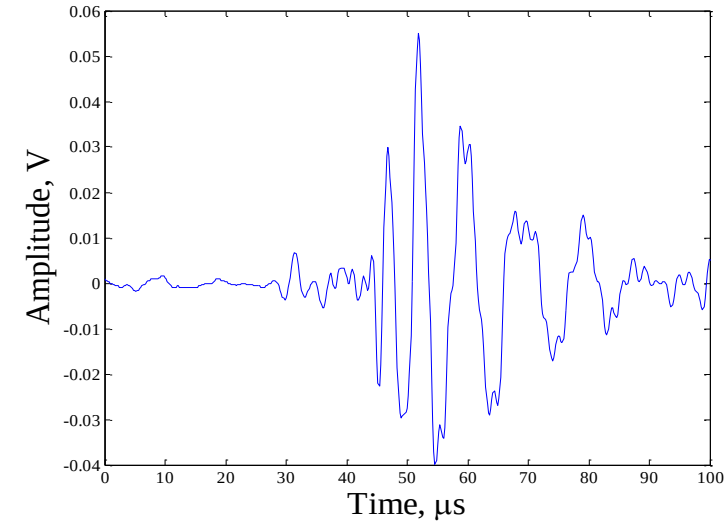

(a)

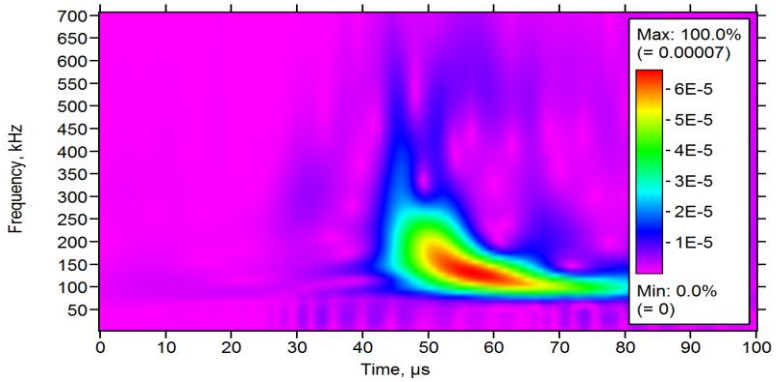

(b)

Figure 3.20. (a) Surface crack growth signal from wafer sensor (b) wavelet analysis of the acoustic emission signal

During these tests, the crack growth initially was slow and it accelerated as the crack length increased. For analyzing these events, the acoustic emission data was divided roughly into four quarters of the entire test duration. The acoustic emission amplitude distribution plots for the four channels were plotted for each of the four segments of the fatigue test as shown in Figure 3.21 below. Channel 1 and 4 are connected to the resonant sensors, channel 2 to the shear sensor array, while channel 3 is connected to the bonded piezoelectric sensor.

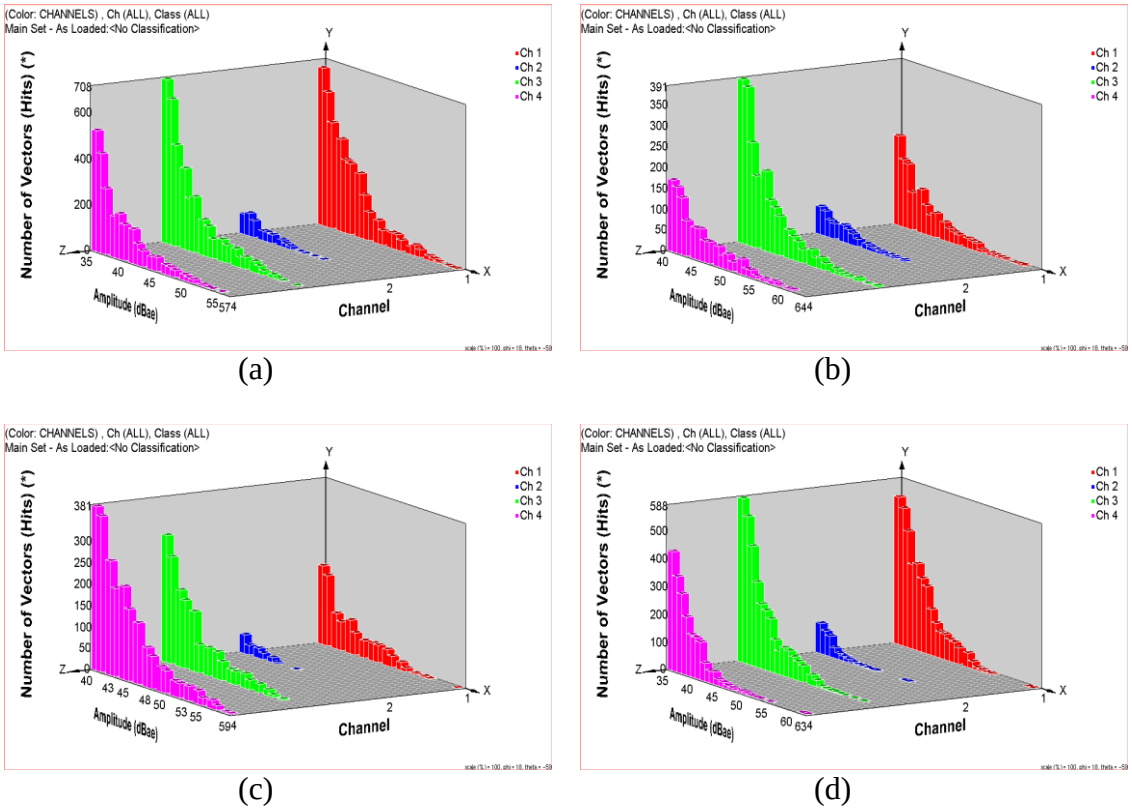

Figure 3.21. Amplitude distribution for the aluminum specimen after, (a) 1st quarter (b) 2nd quarter (c) 3rd quarter (d) 4th quarter of the fatigue test

From Figure 3.21, it can be seen that the acoustic emission activity in terms of number of events at all amplitudes were high during the first quarter (Figure 3.21(a)) of the fatigue life, then in the second and third quarter the number of events at each channel decreased then increased in the last quarter. Channel 2 generally had lower number of events than channel 1, 3 and 4 because the shear sensor had lower sensitivity and only acquired signals generated from fatigue crack source, while the PZT wafer acquire signals from a variety of sources other than fatigue crack growth, such as noise and friction.

Next three dimensional scatter plots in which each acoustic emission event is represented in terms of its amplitude, rise time and duration in a three dimensional space as shown in Figure 3.22. It can be seen that for channel 2 (Figure 3.22(a)), which is connected to the shear sensor, the cluster of events with short rise time (less than 25 μs) and short duration (less than 100 μs) and amplitude between 40 dB and 50 dB. Since the shear component has high frequency and is non-dispersive it was expected that shear sensor would have shorter rise time. Channel 3, which is connected to the PZT wafer, had two clusters of noticeable events (Figure 3.22(b)). The first cluster had shorter rise time with shorter duration, while the second cluster had larger rise time with longer durations of more than 200 μs.

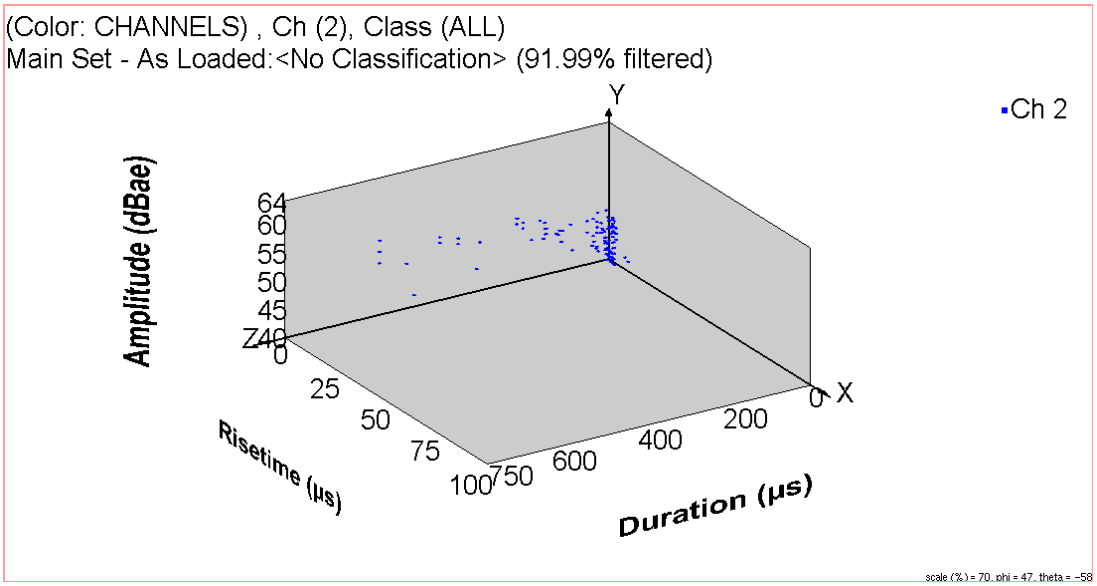

(a)

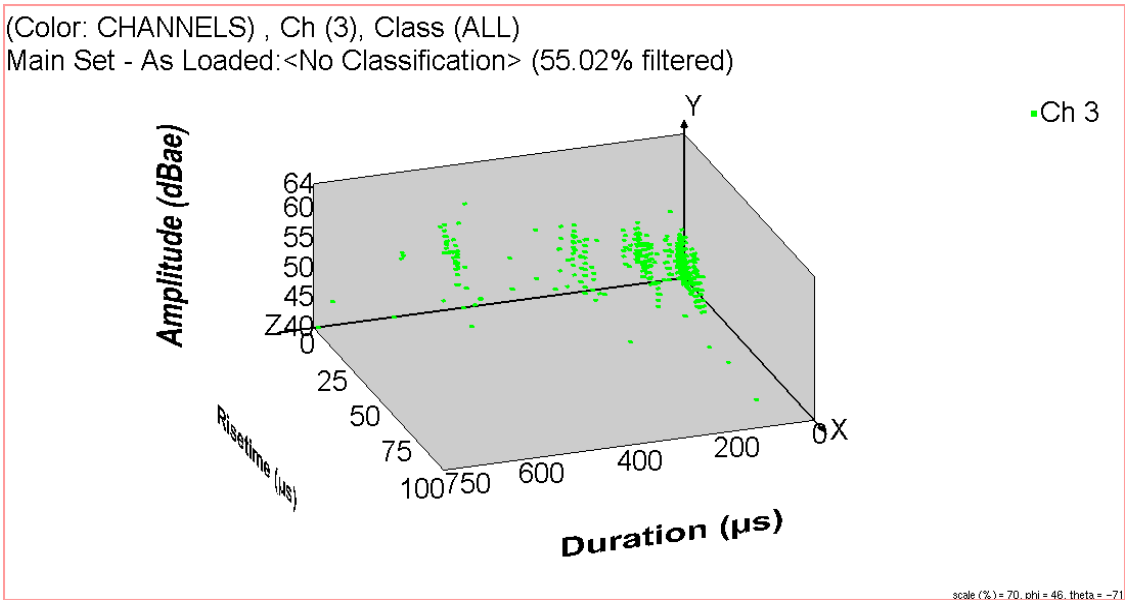

(b)

Figure 3.22. Three dimensional plot of Amplitude, rise time and duration for (a) Channel 2 (b) Channel 3

CHAPTER 4

SIMULATED CRACK GROWTH IN ALUMINUM PLATES

In order to provide a better understanding of acoustic emission waveforms, in particular the shear horizontal component, numerical analysis of stress wave propagation was performed. The finite element simulations shed light on how the waveforms changed with the source sensor distance and angular orientation.

4.1 Material Properties

The aluminum plate specimen was modeled as an isotropic material, with elastic properties corresponding to 2024-T3 aluminum (Bauccio & American Society for Metals., 1993) and are listed in Table 4.1. The Loctite super glue which was used to affix the piezoelectric sensor to the aluminum plate was modeled with dimensions 10mm × 2mm × 0.1mm. The material properties for Loctite superglue and piezoelectric sensors are provided in Table 4.2 and Table 4.3 respectively.

Table 4.1. 2024-T3 aluminum material properties

Physical Properties	Metric
Density, ρ, kg/m^3	2780
Tensile Yield Strength, MPa	345
Ultimate Tensile Strength, MPa	483
Modulus of Elasticity, *E*, GPa	73.1
Poisson's Ratio, ν	0.33

Table 4.2. Loctite superglue material properties used for numerical simulation

Physical Properties	Metric
Density, ρ, kg/m^3	1380
Modulus of Elasticity, *E*, GPa	3.24
Poisson's Ratio, ν	0.4

Table 4.3. Piezoelectric material properties used for numerical simulation

Physical Properties	Metric
Density, ρ, kg/m^3	7800
Modulus of Elasticity, *E*, GPa	55
Poisson's Ratio, ν	0.38

4.2 Finite Element Model

A three dimensional aluminum plate specimen containing a central crack under tensile loading was modeled using Virtual Proving Ground (VPG) preprocessor. The finite element model is a complete replication of the actual physical plate with dimensions 600mm × 300mm × 3mm. Two shear sensors were also modeled unto the surface of the plate with dimensions 10mm × 2mm × 0.5 mm. The shear sensors, which were perpendicular to each other, were along the radii of 150mm away from the fracture tip at 45 degrees orientation from the line of symmetry.

Figure 4.1(a) shows the location of the acoustic emission impulse which is at the center of the plate along the mid-plane and Figure 4.1(b) illustrates the location of the shear sensors with respect to the source of impulse. Crack growth related acoustic emission signals were simulated using a short triangular impulse located at point between C and F on the free edge of the plate specimen as shown in Figure 4.1(a).

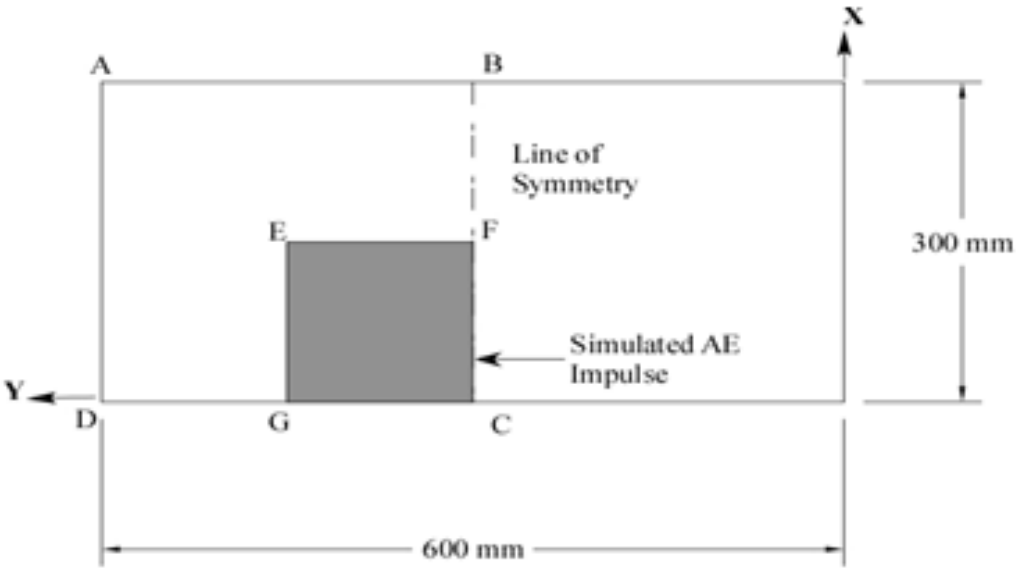

(a)

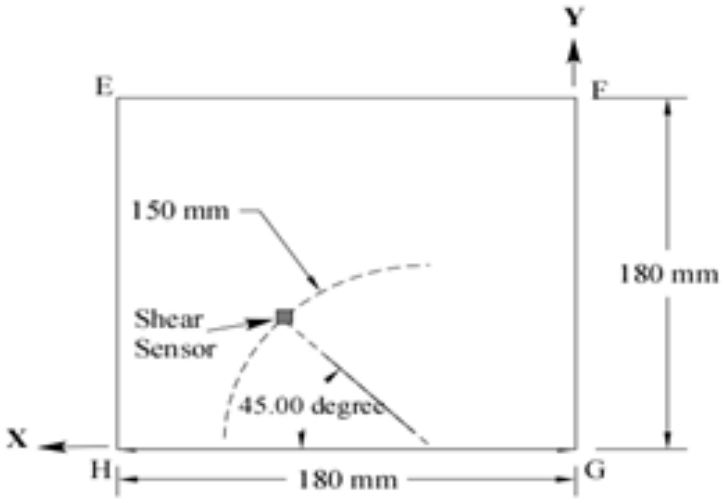

(b)

Figure 4.1. Flat plate finite element model showing (a) location of impulse and (b) distance and orientation to the sensors

The short triangular impulse lasted for 1 μs with peak load amplitude of 1000N applied along the neutral axis at the center of the plate. The triangular pulse load curve is shown in Figure 4.2 below.

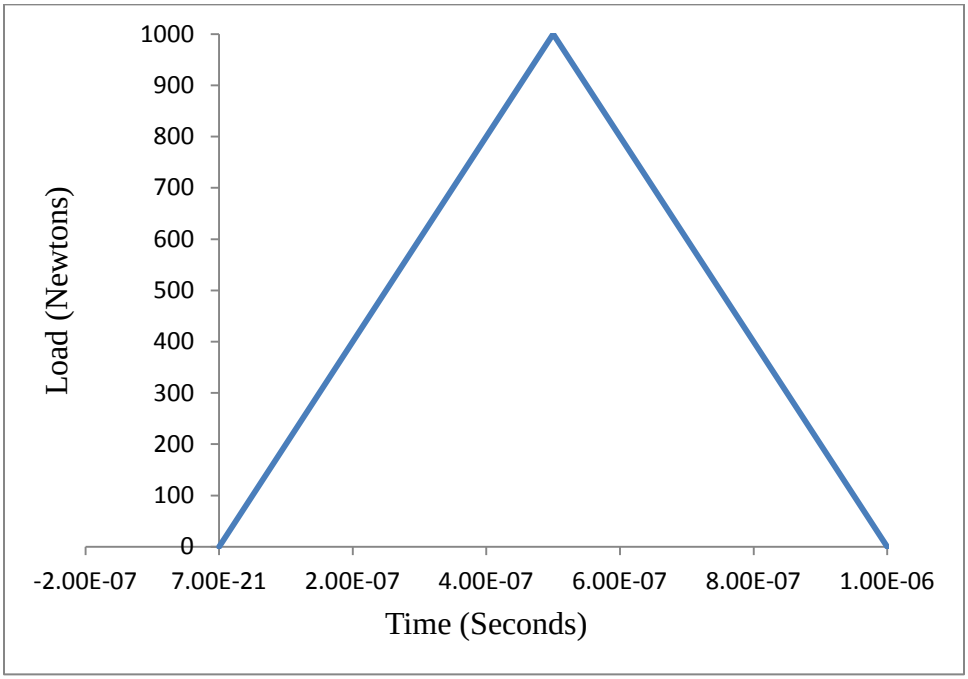

Figure 4.2. Triangular pulse load curve diagram

Half of the 600mm long, 300mm wide, and 3mm depth plate was modeled using 8 node brick elements. Only the left half portion of the aluminum plate was modeled, making the right edge symmetrical to the line BC shown in Figure 4.1(a). Temporal and spatial resolution was taken into consideration in order to accurately represent ultrasonic waves with frequencies up to 1 MHz. A high time resolution (10 nanosecond step time) and small element size were used. In this study, a mesh element size of 0.6mm × 0.6mm × 0.6mm was used in the EFCG area where the working shear sensors are located which

is shown in Figure 4.1(a) above. For the remaining ABCD plate area, coarser mesh was used mainly to reduce computational time, as shown in Figure 4.3 below.

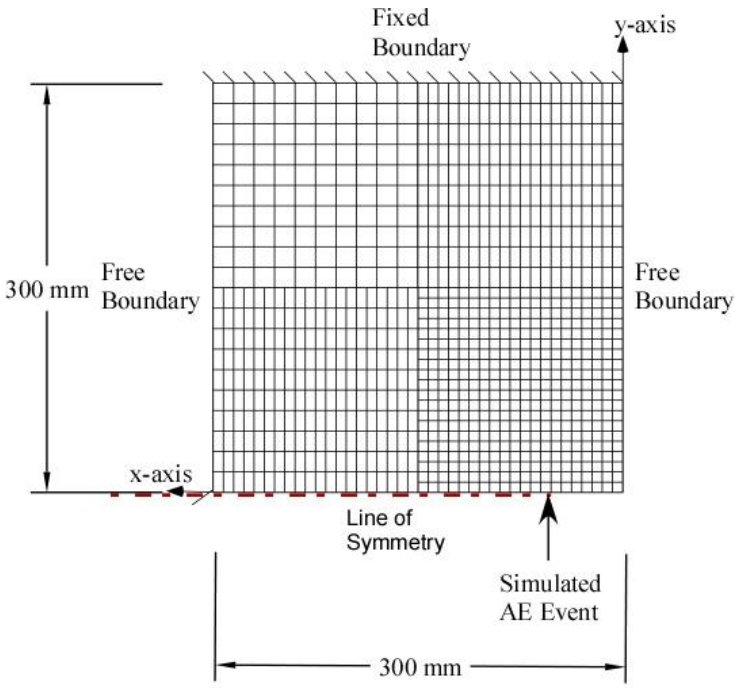

Figure 4.3. Illustration of finite element mesh grid used for the simulation showing a denser mesh in the area of the simulated impulse

4.3 Finite Element Results

In this chapter, combinations of different impulse location and duration with respect to the neutral axis were studied. Most of the results included in this chapter are from impulses located at the neutral axis, which represents a crack growth occurring around the center of the plate thickness. Also included, are results corresponding to an impulse located at the surface of the aluminum plate specimen.

Frames from animation of the propagating wave on the top surface of the area ABCD in Figure 4.1(a) are shown in Figure 4.4 at different time intervals after the simulated acoustic emission event was applied at the neutral axis of the plate. The fringes corresponding to the y-stress component are shown in these frames.

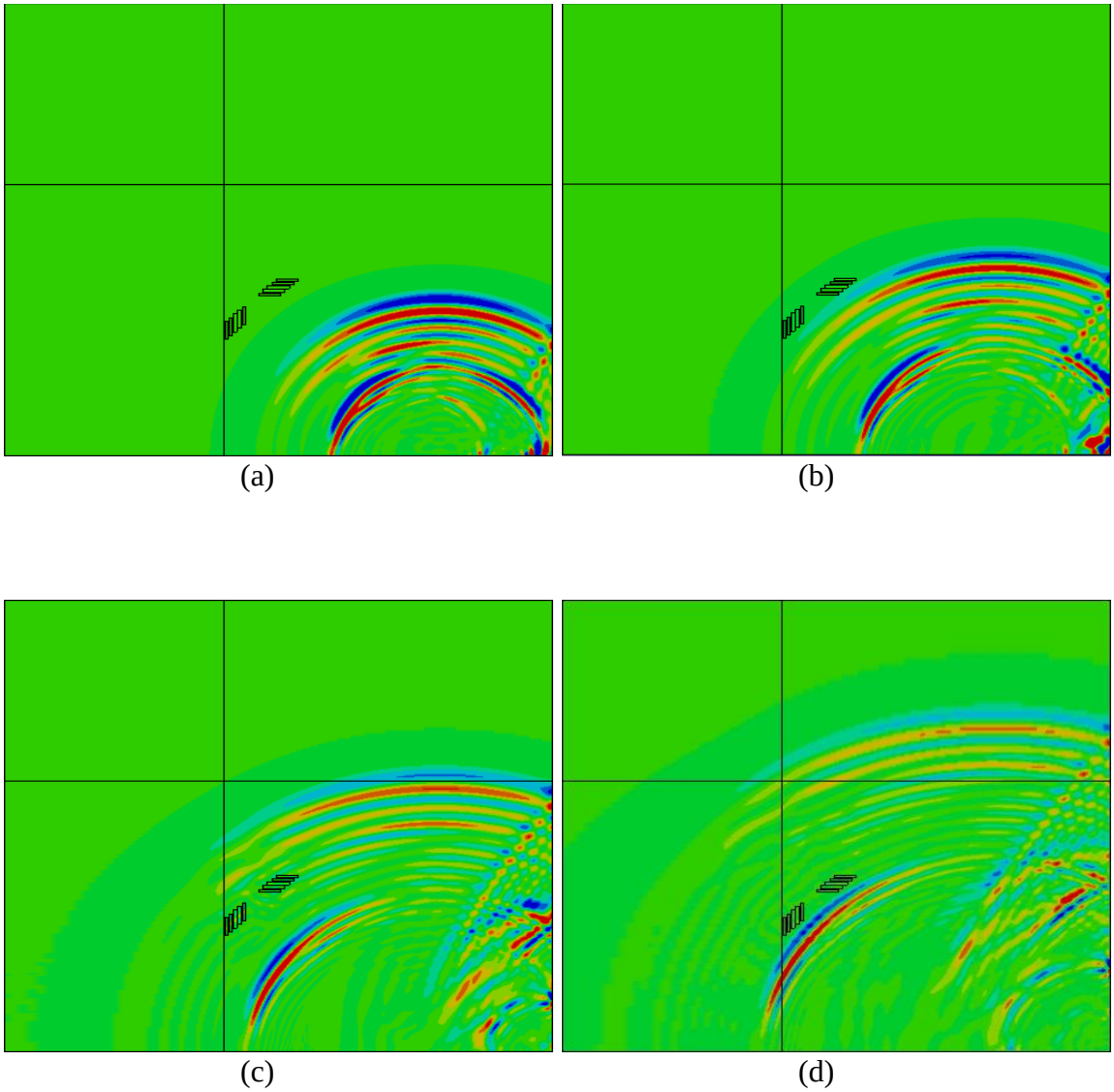

(a) (b)

(c) (d)

Figure 4.4. Visualization of the propagation of stress waves at different times after impulse (a) 20 μs (b) 25 μs (c) 35 μs (d) 43 μs

The alternating tensile and compressive wave fronts in the stress wave are seen as blue and red arcs in Figure 4.4(a) and Figure 4.4(b). Two distinct groups of waves can be seen as they separate into well recognizable groups in Figure 4.4(c) and Figure 4.4(d). The first group corresponds to the S_0 mode, while the second group corresponds to the shear horizontal mode (SH_0) of wave propagation in plates. Figure 4.5(a) and Figure 4.5(b) below shows acoustic emission waveforms along with its wavelet analysis from the finite analysis performed where the load impulse was at the neutral axis. The second amplitude peak at 300μs was from reflections that resonated between shear sensor arrays.

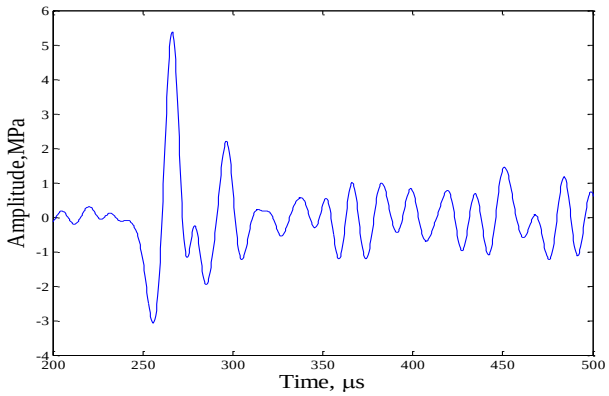

(a)

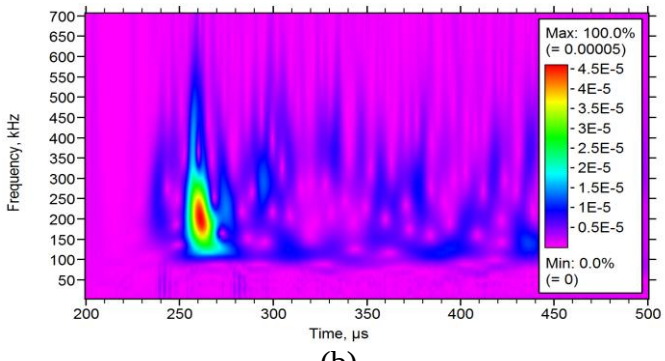

(b)

Figure 4.5. (a) Acoustic waveform from finite element shear sensor, impulse at neutral axis (b) corresponding wavelet analysis

Figure 4.6(a) below shows acoustic emission waveforms along with its wavelet analysis from the finite analysis performed where the load impulse was located 0.25mm from the neutral axis (Figure 4.6(b)). The peak amplitude of the SH component is 5MPa at a frequency of approximately 210 kHz.

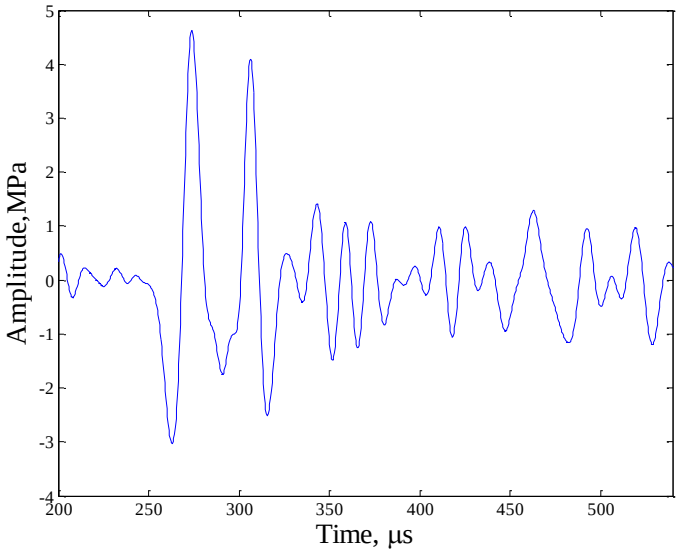

(a)

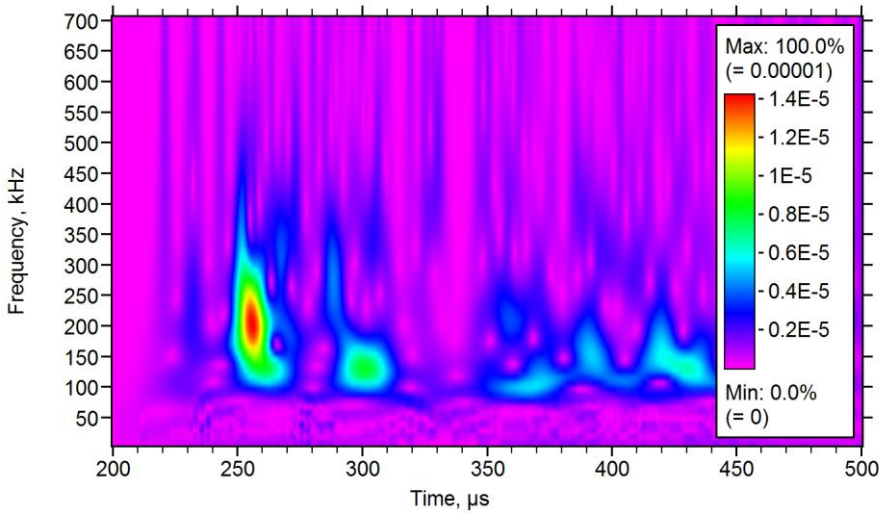

(b)

Figure 4.6. (a) Acoustic waveform from finite element shear sensor, impulse located 0.25mm from neutral axis (b) corresponding wavelet analysis

Figure 4.7(a) below, shows acoustic emission waveforms along with its wavelet analysis (Figure 4.7(b)) from the finite analysis performed where the load impulse was located at the surface edge. The shear horizontal component occurred at 260 μs following a second amplitude of 4MPa that occurred around 320 μs. The frequency component of the SH component is approximately 230 kHz which is shown in Figure 4.7(b).

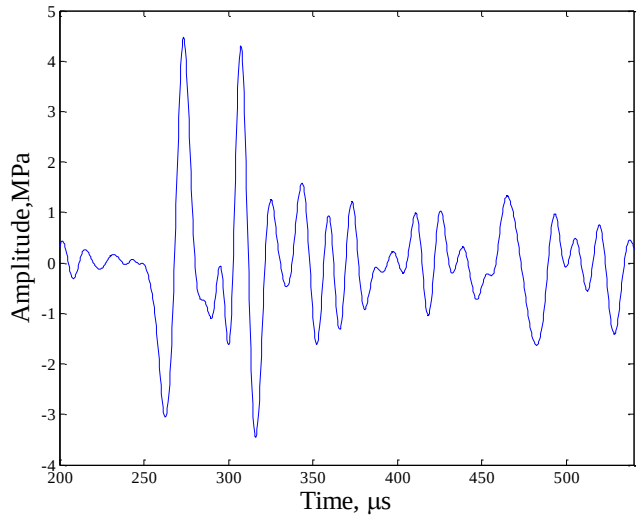

(a)

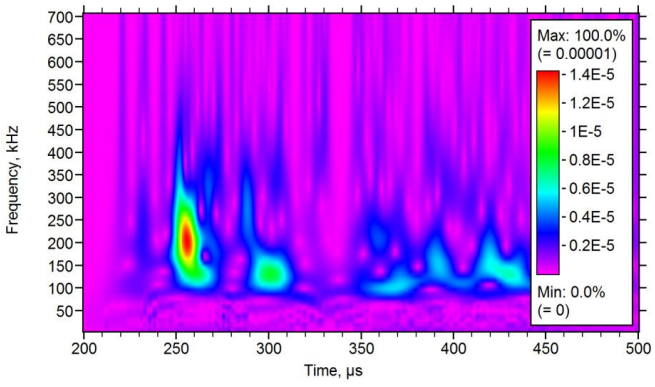

(b)

Figure 4.7. (a) Acoustic waveform from finite element shear sensor, impulse located at surface edge (b) corresponding wavelet analysis

CHAPTER 5

CONCLUSION

The shear sensor array has been shown to clearly capture the shear mode of acoustic emission during both pulser simulation of acoustic emissions and the actual acoustic emissions emanating from the tip of a crack propagating due to cyclical loading. Commercial type sensors are more sensitive to asymmetrical component of the acoustic emission waveform and most noise signals (friction) have large A_0. Bonded wafers are less sensitive to A_0 and hence have better noise performance, but both are incapable of detecting SH_0 component of the acoustic emission waveform.

The new capability to preferentially detect SH_0 component while suppressing the other components holds promise to efficiently minimize false positives during AE based structural health monitoring. The shear sensor array performance could be further improved to provide greater ratio of sensitivity to SH_0 component. The electrical connections to the sensors, the paths to ground, and electrical shielding are all being refined in an effort to reduce electrical noise in the signals. In addition to the electrical noise, the shear sensor array's observed increase in noise and decreased sensitivity to the shear component during the later stages of the cyclical loading tests is believed to be a result of degraded bonding between the shear sensor array and the aluminum specimen.

REFERENCES

Bauccio, M., & American Society for Metals. (1993). *ASM metals reference book* (3rd ed.). Materials Park, Ohio: ASM International.

Cady, W. G. (1964). *Piezoelectricity; an introduction to the theory and applications of electromechanical phenomena in crystals*. New York: Dover Publications.

Chang, F.-K., United States. Air Force. Office of Scientific Research., United States. Army Research Office, & National Science Foundation (U.S.). (1997). *Structural health monitoring : current status and perspectives : proceedings of the International Workshop on Structural Health Monitoring : Stanford University, Stanford, CA, September 18-20, 1997*. Lancaster, Pa.: Technomic Pub.

Cuc, A., Giurgiutiu, V., Joshi, S., & Tidwell, Z. (2007). Structural health monitoring with piezoelectric wafer active sensors for space applications. *Aiaa Journal, 45*(12), 2838-2850.

Dowling, N. E. (2007). *Mechanical behavior of materials : engineering methods for deformation, fracture, and fatigue*. Upper Saddle River, NJ: Pearson Prentice Hall.

Dowling, N. E. (2009). Mean stress effects in strain-life fatigue. *Fatigue & Fracture of Engineering Materials & Structures, 32*(12), 1004-1019.

Dunegan, H. L. (August 2000). *The DECI Report: An alternative to pencil lead breaks for simulation of acoustic emission signal sources*.

Dunegan, H. L., Hartman, W. F., & American Society for Nondestructive Testing. (1981). *Advances in acoustic emission : proceedings of International Conference on Acoustic Emission, held in Anaheim, California, September, 1979*. Knoxville, Tenn. (P.O. Box 22532, Knoxville 37922): Dunhart Publishers.

Giurgiutiu, V., Bao, J., & Zhao, W. (2003). Piezoelectric wafer active sensor embedded ultrasonics in beams and plates. [Article]. *Experimental Mechanics, 43*(4), 428-449.

Gorman, M. R. (1991). PLATE WAVE ACOUSTIC-EMISSION. [Article]. *Journal of the Acoustical Society of America, 90*(1), 358-364.

Graff, K. F. (1991). *Wave Motion in Elastic Solid*. New York: Dover Publications.

Grondel, S., Delebarre, C., Assaad, J., Dupuis, J. P., & Reithler, L. (2002). Fatigue crack monitoring of riveted aluminium strap joints by Lamb wave analysis and acoustic emission measurement techniques. *Ndt & E International, 35*(3), 137-146.

Jaffe, B., Cook, W. R., & Jaffe, H. L. (1971). *Piezoelectric ceramics*. London; New York: Academic Press.

Lamb, H. (1904). On the propagation of tremors over the surface of an elastic solid. *Philosophical Transactions of the Royal Society of London Series a-Containing Papers of a Mathematical or Physical Character, 203*, 1-42.

Mason, W. P. (1960). *Piezoelectric crystals and their application to ultrasonics*. Princeton (N.J.) [u.a.]: Van Nostrand.

Mickens, T., Schulz, M., Sundaresan, M., Ghoshal, A., Naser, A. S., & Reichmeider, R. (2003). STRUCTURAL HEALTH MONITORING OF AN AIRCRAFT JOINT. *Mechanical Systems and Signal Processing, 17*(2), 285-303.

Miller, G. F., & Pursey, H. (1955). On the Partition of Energy between Elastic Waves in a Semi-Infinite Solid. *Proceedings of the Royal Society of London. Series A, Mathematical and Physical Sciences, 233*(1192), 55-69.

Rose, J. L. (1999). *Ultrasonic waves in solid media*. Cambridge: Cambridge University Press.

Thyagarajan, S. K., Schulz, M. J., Pai, P. F., & Chung, J. (1998). DETECTING STRUCTURAL DAMAGE USING FREQUENCY RESPONSE FUNCTIONS. *Journal of Sound and Vibration, 210*(1), 162-170.

Viktorov, I. A. (1967). *Rayleigh and Lamb waves: physical theory and applications*. New York,: Plenum Press.

Waanders, J. W. (1991). *Piezoelectric ceramics : properties and applications*. Eindhoven, Netherlands; Mackeyville, Pa.: Philips Components ; Distributed by American Piezo Ceramics].

Wang, L., & Yuan, F. G. (2007). Group velocity and characteristic wave curves of Lamb waves in composites: Modeling and experiments. *Composites Science and Technology, 67*(7-8), 1370-1384.

Worlton, D. C. (1961). EXPERIMENTAL CONFIRMATION OF LAMB WAVES AT MEGACYCLE FREQUENCIES. *Journal of Applied Physics, 32*(6), 967-&.

Zhang, H., Schulz, M. J., Naser, A., Ferguson, F., & Pai, P. F. (1999). STRUCTURAL HEALTH MONITORING USING TRANSMITTANCE FUNCTIONS. *Mechanical Systems and Signal Processing*, *13*(5), 765-787.

APPENDIX A

MATLAB CODE FOR PULSER SIMULATION

```
n1=load ('1.txt');
n2=load ('2.txt');
n3=load ('3.txt');
n4=load ('4.txt');
n5=load ('5.txt');
n8=load ('8.txt');
n9=load ('9.txt');
n10=load ('10.txt');
n11=load ('11.txt');
n12=load ('12.txt');
n13=load ('13.txt');
n14=load ('14.txt');
n15=load ('30degrees.txt');
n16=load ('45degrees.txt');
n17=load ('60degrees.txt');
time=n1(:,1);
ampl=n1(:,2);
ampl2=n2(:,2);
ampl3=n3(:,2);
ampl15=n15(:,2);
ampl16=n16(:,2);
ampl17=n17(:,2);
ampl14=n14(:,2);
plot(time*1e6,ampl15);xlabel 'Time, \mus';ylabel 'Amplitude, V';
figure(2)
plot(time*1e6,ampl16);xlabel 'Time, \mus';ylabel 'Amplitude, V';
figure(3)
plot(time*1e6,ampl17);xlabel 'Time, \mus';ylabel 'Amplitude, V';
figure (4)
plot(time*1e6,ampl14);xlabel 'Time, \mus';ylabel 'Amplitude, V';
```

APPENDIX B

MATLAB CODE FOR NUMERICAL SIMULATION

```
n1=load ('x.txt');
n2=load ('y.txt');
n3=load ('0.25_NA_Xstress.txt');
n4=load ('0.25_NA_Ystress.txt');
n5=load ('Close_Spacing.txt');
time=n1(:,1);
time2=n3(:,1);
time3=n5(:,1);
ampl=n1(:,2);
ampl2=n2(:,2);
ampl3=n3(:,2);
ampl4=n4(:,2);
NA=ampl4-ampl3;
surface=ampl2-ampl;
plot(time*1e6,ampl2);xlabel 'Time, \mus';ylabel 'Amplitude, MPa';
```

APPENDIX C

MATLAB CODE FOR RESAMPLING NUMERICAL DATA

```
% Input the experimental crack signals
clc
clear
n1 = load('Surface.txt'); %rectangular pulse signal from simulation%
don't forget to specify location

%%%%%%%%%%%%%%%%%% plot of the waveforms %%%%%%%%%%%%%%%%%%

x=n1(:,1);%x-coordinate values
y=n1(:,2);%y-coordinate values
v=0;%initializing the intermediate values
j=1;%index for matrix of interpolated values
m=0;%initializing the matrix for interpolated values

for i=1:1400
    if x(i)== v
        m(j)=y(i);
        j=j+1;
        v=v+2E-7;
    else if (x(i)<= v)&&(x(i+1)>= v)
        m(j)=((v-x(i))/(x(i+1)-x(i)))*(y(i+1)-y(i))+y(i);
        j=j+1;
        v=v+2E-7;%sample time
        else
            a = 1;
        end
    end
end
m'
%numerical signal resampled at 0.2 µs that is the same as crack%
```